Assessing the Performance of an Industrial SBCR for Fischer–Tropsch Synthesis: Experimental and Modeling

Laurent Sehabiague, Omar M. Basha, Yemin Hong, and Badie Morsi
Dept. of Chemical and Petroleum Engineering, University of Pittsburgh, Pittsburgh, PA 15261

Zhansheng Shi
National Institute of Clean-and-Low-Carbon Energy, Beijing 102209, P.R. China

Dept. of Chemical Engineering, Beijing Key Laboratory of Green Chemical Reaction Engineering and Technology, Tsinghua University, Beijing 100084, P.R. China

Haolin Jia, Li Weng, Zhuowu Men, and Ke Liu
National Institute of Clean-and-Low-Carbon Energy, Beijing 102209, P.R. China

Yi Cheng
Dept. of Chemical Engineering, Beijing Key Laboratory of Green Chemical Reaction Engineering and Technology, Tsinghua University, Beijing 100084, P.R. China

DOI 10.1002/aic.14931
Published online July 14, 2015 in Wiley Online Library (wileyonlinelibrary.com)

The main objective of this study is to predict the performance of an industrial-scale (ID = 5.8 m) slurry bubble column reactor (SBCR) operating with iron-based catalyst for Fischer–Tropsch (FT) synthesis, with emphasis on catalyst deactivation. To achieve this objective, a comprehensive reactor model, incorporating the hydrodynamic and mass-transfer parameters (gas holdup, ε_G, Sauter-mean diameter of gas bubbles, d_{32}, and volumetric liquid-side mass-transfer coefficients, k_La), and FT as well as water gas shift reaction kinetics, was developed. The hydrodynamic and mass-transfer parameters for He/N_2 gaseous mixtures, as surrogates for H_2/CO, were obtained in an actual molten FT reactor wax produced from the same reactor. The data were measured in a pilot-scale (0.29 m) SBCR under different pressures (4–31 bar), temperatures (380–500 K), superficial gas velocities (0.1–0.3 m/s), and iron-based catalyst concentrations (0–45 wt %). The data were modeled and predictive correlations were incorporated into the reactor model. The reactor model was then used to study the effects of catalyst concentration and reactor length-to-diameter ratio (L/D) on the water partial pressure, which is mainly responsible for iron catalyst deactivation, the H_2 and CO conversions and the C_{5+} product yields. The modeling results of the industrial SBCR investigated in this study showed that (1) the water partial pressure should be maintained under 3 bars to minimize deactivation of the iron-based catalyst used; (2) the catalyst concentration has much more impact on the gas holdup and reactor performance than the reactor height; and (3) the reactor should be operated in the kinetically controlled regime with an L/D of 4.48 and a catalyst concentration of 22 wt % to maximize C_{5+} products yield, while minimizing the iron catalyst deactivation. Under such conditions, the H_2 and CO conversions were 49.4% and 69.3%, respectively, and the C_{5+} products yield was 435.6 ton/day. *AIChE J*, 61: 3838–3857, 2015
Keywords: slurry bubble column reactor, Fischer–Tropsch, hydrodynamics, mass transfer, modeling, scale-up

Introduction and Background

In Fischer–Tropsch (FT) synthesis, the syngas ($CO + H_2$) is converted into synthetic hydrocarbon products in the presence of a catalyst, conventionally iron or cobalt. This synthesis is a combination of oligomerization reactions to produce mainly paraffins with typical H_2/CO ratios between 2.06 and 2.16.[1,2] The FT reactions and the water gas shift (WGS) side reaction have been reported to be exothermic ($\Delta H^\circ_{FT} = -165$ kJ/mol at 298 K[3] and $\Delta H^\circ_{WGS} = -41.2$ kJ/mol at 298 K[4]). The FT syntheses, carried out at high (>300°C) and low (<300°C) temperatures, are known as high-temperature FT (HTFT) and low-temperature FT (LTFT), respectively. The HTFT synthesis is usually carried out in Fluidized-bed or circulating-bed reactors to produce volatile hydrocarbons, such as gasoline. The LTFT synthesis is carried out in Fixed-bed reactors (FBRs) or slurry bubble column reactors (SBCRs) to produce heavier hydrocarbons, which upon upgrading, yield a variety of high-value products, ranging from jet and diesel fuels to lubricating oil and candle wax. SBCRs have numerous advantages over FBRs,[2,5] including better temperature control and heat removal; lower capital cost; lower pressure drop; ability

Correspondence concerning this article should be addressed to B. Morsi at morsi@pitt.edu.

Table 1. Literature Studies on the Hydrodynamic and Mass-Transfer Parameters in F-T SBCRs

References	Gas-Liquid-Solid System	Reactor Geometry (m)	Operating Conditions U_G (m/s); P (bar); T (K)	Parameter Measured
Deckwer et al.[8]	N_2 Paraffin Wax Al_2O_3	$D_C = 0.04, 0.1$	P up to 11 T: 416 & 543 U_g up to 0.04 d_p: up to 5 μm C_S up to 16 wt %	ε_g, k_La
Bukur et al.[9–12], Daly et al.,[13] and Patel et al.[14]	N_2 FT-300 Paraffin Wax, Sasol Arge wax, Mobil reactor wax Iron Oxide, Silica	$D_C = 0.05, 0.21$ $H_C = 3$	P_{atm} T: up to 538 U_g: up to 0.15 U_l: 0–0.02 d_p: up to 44 μm C_S: 10–30 wt %	ε_g, d_S
Krishna et al.[15]	Air Paraffin Oil Silica	$D_C = 0.38$	P_{atm} T_{amb} U_g up to 0.5 C_V: up to 36 vol %	ε_g
Vandu et al.[16]	Air C_9–C_{11} Paraffin Oil Puralox (Al_2O_3)	$D_C = 0.1$	P_{atm} T_{amb} U_g up to 0.4 C_V up to 25 vol %	ε_g, k_La
Woo et al.[17]	Actual F-T reactive system with Al_2O_3 supported Co catalyst	$D_C = 0.05$ H_C =1.5	P: 10–30 T: 480–520 U_g: 0.017–0.136 C_S: 9–27 wt %	ε_g
Behkish et al.[18,19]	H_2, CO, N_2, He, CH_4 Isopar-M Glass Beads, Al_2O_3	$D_C = 0.3$ $H_C = 3$	P up to 30 T up to 473 U_g up to 0.39 C_V up to 36 vol %	ε_g, d_S, k_La
Sehabiague and Morsi[20]	N_2, He C_{12}–C_{13} Paraffin Oil, Light F-T Cut, Heavy F-T Cut Iron oxide, Al_2O_3	$D_C = 0.3$ $H_C = 3$	P up to 30 T up to 530 U_g up to 0.26 C_V up to 20 vol %	ε_g, d_{32}, k_La

to use finer catalyst particles (<100 μm), higher yield per reactor volume, and fewer necessary shutdowns as catalyst can be continuously added to or removed from the reactor. Despite these advantages, however, SBCRs inherit some drawbacks, such as strong liquid back-mixing, significant catalyst attrition; challenging catalyst separation from the heavy products; and complex hydrodynamics.

The design and scale-up of SBCRs require, among others, accurate details of the hydrodynamics, gas-liquid-solid heat and mass-transfer parameters, and reaction kinetics, including catalyst deactivation. These data should be determined under typical FT conditions, that is, pressures up to 10–45 bar and temperatures up to 210–260°C. Also, these data should be measured under high gas throughput (up to 0.5 m/s) in a large-scale reactor [up to 10-m industrial-scale (ID)] operating with high slurry concentration (up to 50 wt %) for ensuring process intensification and high space-time yields in commercial SBCRs. Wilkinson et al.[6] reported that to avoid wall effects and obtain representative data for scale-up purposes, the hydrodynamic data should be obtained in reactors with ID > 0.15 m, since the gas holdup was found, in several cases, to be independent of the reactor inside diameter. Moustiri et al.,[7] however, reported significant changes in the reactor behavior with diameters between 0.15 and 0.2 m.

Literature studies on the hydrodynamic and mass-transfer parameters in FT liquids, briefly summarized in Table 1, indicate that most of the data were obtained in small-size reactors, except for Bukur et al.,[9–12] Daly et al.,[13] and Patel et al.,[14] Behkish et al.,[18,19] Sehabiague and Morsi,[20] and Krishna et al.,[15] who used reactors with inside diameters >0.15 m. Bukur et al.,[9–12] Daly et al.,[13] and Patel et al.[14] performed experiments in a SBCR (0.21-m ID and 3-m height) provided with perforated plate and bubble cap distributors, and measured the gas holdup, Sauter mean bubble diameter, solids dispersions as well as flow regime transitions for N_2 in Sasol wax and FT-300 wax in the presence of iron oxide (0–5 μm) and silica (20–44 μm) under elevated temperatures (538 K) and ambient pressure. Behkish et al.,[18,19] Sehabiague and Morsi,[20] conducted their experiments in a 0.29-m ID, 3-m height column in a three-phase FT system under both elevated pressures and temperatures, and investigated the effect of various operating parameters on the gas holdup, bubble size, and volumetric mass-transfer coefficients. Krishna et al.,[15] however, carried out their experiments under ambient conditions, which are far from those used in actual FT synthesis. Moreover, the values and behavior of the hydrodynamic and mass-transfer parameters reported in various FT liquids appeared to be strongly dependent on the nature of the liquids used. Thus, there is a great need to obtain accurate hydrodynamic and mass-transfer parameters data using actual FT reactor cuts under typical FT conditions.

The main objective of this study is to predict the performance (CO and H_2 conversion and C_{5+} products yield) of an industrial-scale (ID = 5.8 m) SBCR operating with iron-based catalyst for FT synthesis, with emphasis on factors affecting catalyst deactivation. To achieve this objective, a comprehensive reactor model, incorporating the hydrodynamic and mass-transfer parameters (gas holdup, ε_G, Sauter-mean diameter of gas bubbles, d_{32}, and volumetric liquid-side mass-transfer coefficients, k_La), and FT as well as WGS reaction kinetics, was developed. To solve the model equations, precise knowledge of the hydrodynamic and mass-transfer parameters obtained under actual conditions, and FT as well as WGS reaction kinetics are required, keeping in mind that the FT SBCR should be operated under isothermal conditions. The model will then be used to predict the effects of catalyst concentrations and reactor heights on the reactor performance and the

Table 2. Material Balance Equations

Phase	Material Balance Equation	
Liquid	$\frac{d}{dz}\left(\varepsilon_{\mathrm{L}} D_{\mathrm{L}} \frac{dC_{i,\mathrm{L}}}{dz}\right) - \frac{d\left(U_{\mathrm{L}} C_{i,\mathrm{L}}\right)}{dz} + \varepsilon_{\mathrm{L}} (k_{\mathrm{L}} a_{\mathrm{L}})_{i,\mathrm{LB}} \left(C^{*}_{i,\mathrm{LB}} - C_{i,\mathrm{L}}\right) + \varepsilon_{\mathrm{L}} (k_{\mathrm{L}} a_{\mathrm{L}})_{i,\mathrm{SB}} \left(C^{*}_{i,\mathrm{SB}} - C_{i,\mathrm{L}}\right) + \varepsilon_{\mathrm{L}} R_i = 0$	(1)
Small Bubbles	$\frac{d}{dz}\left(\varepsilon_{SB} D_{SB} \frac{dC_{i,SB}}{dz}\right) - \frac{d\left(U_{G,SB} C_{i,SB}\right)}{dz} - \varepsilon_{L} (k_{L} a_{L})_{i,SB} \left(C^{*}_{i,SB} - C_{i,L}\right) + \frac{K}{L}\left(U_{\mathrm{G},LB} - U_{\mathrm{G},SB}\right)\left(C_{i,\mathrm{SB}} - C_{i,\mathrm{LB}}\right) = 0$	(2)
Large Bubbles	$\frac{d}{dz}\left(\varepsilon_{LB} D_{LB} \frac{dC_{i,LB}}{dz}\right) - \frac{d\left(U_{G,LB} C_{i,LB}\right)}{dz} - \varepsilon_{L} (k_{L} a_{L})_{i,LB} \left(C^{*}_{i,LB} - C_{i,L}\right) + \frac{K}{L}\left(U_{G,LB} - U_{G,\mathrm{SB}}\right)\left(C_{i,\mathrm{LB}} - C_{i,\mathrm{SB}}\right) = 0$	(3)
Solid Suspension	$\frac{d}{dz}\left(\varepsilon_{\mathrm{L}} D_{\mathrm{S}} \frac{dC_{\mathrm{S}}}{dz}\right) + \frac{d}{dz}\left(\left(\varepsilon_{\mathrm{L}} U_{\mathrm{P}} - U_{\mathrm{L}}\right) C_{\mathrm{S}}\right) = 0$	(4)

partial pressure of the water produced, which is mainly responsible for the iron-based catalyst deactivation.

Modeling of the FT SBCR

A model for the FT SBCR was developed with the following features: (1) the SBCR is operating in the churn-turbulent flow regime at steady state; (2) the gas is sparged at the bottom of the reactor; (3) the slurry is moving upward at a constant superficial velocity; (4) the catalyst loading inside the reactor is kept constant by adding in the slurry inlet the same amount of catalyst particles that leave the reactor in the slurry outlet; and (5) the heat generated from the reaction is removed using saturated water flowing in bundles of cooling pipes. The model is essentially based on the axial dispersion model in conjunction with the two-class of gas bubbles model.[21] The catalyst particles suspension is modeled using the Sedimentation-Dispersion model. The interactions between the small and large gas bubbles are accounted for in the model using the cross-flow mass exchange term from Rados et al.[22] Furthermore, the following key assumptions were considered: (1) the mass-transfer resistances in the gas-film and in the liquid-solid film are negligible and (2) the slurry temperature is constant. According to these assumptions and model features, the mass balances of each component in the different phases over a differential element of the reactor can be derived as shown in Table 2; and the boundary conditions for solving these equations are given in Table 3.

As can be seen in Table 3, the boundary conditions for the gas and liquid phases at the inlet (bottom) of the reactor are Danckwerts' type[23] conditions. For the solid phase, the average solid concentration in the reactor is kept constant.

The gas consumption and associated decrease of the gas superficial velocity was estimated from an overall mass balance on the gas phase and the pressure profile was obtained from the hydrostatic head pressure

$$-\frac{d\left(U_{\mathrm{G,SB}} \sum_i C_{i,\mathrm{SB}} + U_{\mathrm{G,LB}} \sum_i C_{i,\mathrm{LB}}\right)}{dz} - \sum_i (k_{\mathrm{L}} a_{\mathrm{L}})_{i,\mathrm{SB}} \left(C^{*}_{i,\mathrm{SB}} - C_{i,\mathrm{L}}\right) - \sum_i (k_{\mathrm{L}} a_{\mathrm{L}})_{i,\mathrm{LB}} \left(C^{*}_{i,\mathrm{LB}} - C_{i,\mathrm{L}}\right) = 0 \quad (13)$$

$$\frac{dP}{dz} + \left[\varepsilon_{\mathrm{L}} \rho_{\mathrm{SL}} + \varepsilon_{\mathrm{G}} \rho_{\mathrm{G}}\right] g = 0 \quad (14)$$

More details of the reactor model and the estimation of the different parameters involved in Eqs. 1 through 4 can be found elsewhere.[24,25]

Properties of the Gas-Liquid-Solid Used

The gases used in the experiments were He and N_2 as surrogates for H_2 and CO, respectively. Both gases were purchased from Valley National Gases, USA. The reason for using N_2 and He mixtures in the experiments as surrogates for CO and H_2 mixture is to avoid any chemical reactions between H_2 and CO in the presence of the iron catalyst which will corrupt the solubility values and consequently the corresponding mass-

Table 3. Boundary Conditions

Phase	Boundary Conditions at Bottom		Boundary Conditions at Top	
Liquid	$U_{\mathrm{L}} C_{i,\mathrm{L}} - \varepsilon_{L} D_{\mathrm{L}} \frac{dC_{i,\mathrm{L}}}{dz} = 0$	(5)	$\frac{dC_{i,\mathrm{L}}}{dz} = 0$	(6)
Small Bubbles	$U_{\mathrm{SB}} C_{i,\mathrm{SB}} - \varepsilon_{\mathrm{SB}} D_{\mathrm{SB}} \frac{dC_{i,\mathrm{SB}}}{dz} = U_{\mathrm{SB}} C_{i,\mathrm{G,inlet}}$	(7)	$\frac{dC_{i,\mathrm{SB}}}{dz} = 0$	(8)
Large Bubbles	$U_{\mathrm{LB}} C_{i,\mathrm{LB}} - \varepsilon_{\mathrm{LB}} D_{\mathrm{LB}} \frac{dC_{i,\mathrm{LB}}}{dz} = U_{\mathrm{LB}} C_{i,\mathrm{G,inlet}}$	(9)	$\frac{dC_{i,\mathrm{LB}}}{dz} = 0$	(10)
Solid Suspension	$\frac{\int_0^L C_{\mathrm{S}} dz}{\int_0^L dz} = \overline{C_{\mathrm{S}}}$	(11)	$U_{\mathrm{L}} C_{\mathrm{S,outlet}} = U_{\mathrm{L}} C_{\mathrm{S,inlet}}$	(12)

Table 4. Size Distribution of the Solid Particles Used

Diameter (μm)	Volume % finer than
39	10%
56	30%
80	60%
169	95%

transfer coefficients. Also, experimental data obtained with N_2 and CO as a single component in a one-gallon, high pressure, high temperature agitated autoclave, indicated that N_2 is a perfect surrogate for CO. These two gases, not only have identical molecular weights, but also exhibit almost identical solubilities and mass-transfer coefficients in different FT cuts.[26]

The solid phase used in the experiments is an iron-based catalyst with a skeletal density of 3380 kg/m^3. The particle-size distribution of the catalyst is listed in Table 4 and accordingly the average particle diameter is 81 μm.

The liquid phase used in the experiments is a molten reactor wax, which was produced from the ID SBCR used in this investigation (ID = 5.8 m) using an iron-based catalyst with the particle-size distribution given in Table 4. The wax is a solid at room temperature as its melting point is >90°C. The wax consists mainly of saturated linear paraffins and its estimated molecular weight is 507.64 kg/kmol.

The density, viscosity and surface tension of the molten wax were measured in our laboratory at different temperatures ranging from 380 to 460 K using graduated flasks, Cannon-Fenske routine viscometers and a Fisher Surface Tensiomat, respectively. These experimental data were modeled as a function of temperature and predictive correlations were developed. The vapor pressure was predicted with the Asymptotic Behavior Correlations developed by Marano and Holder,[27,28] assuming the wax composition consists mainly of linear paraffins. From the values obtained a simple equation was developed for calculating the vapor pressure as a function of temperature. The correlations for predicting the physical properties of the molten reactor wax as a function of temperature are grouped in Table 5 and comparisons between the predicted and experimental values are shown in Figure 1. It should be noted that the molten reactor wax used in this study has comparable physical properties to those of the molten paraffin wax used by Deckwer et al.[8,29] who reported a density of 670 kg/m^3, a viscosity of 2.0 mPa·s and a surface tension of 0.021 N/m at 523 K.

Experimental Setup

In this study, a pilot-scale SBCR (ID = 0.29 m and height = 3 m) was used to measure the hydrodynamic and mass-transfer parameters, and therefore the wall effects should be negligible. Such data would be valid for scale-up purposes, since no corrections are needed for pressure, temperature, reactor size, or system nature. Photos of the reactor and spider-type gas distributor, which contains 108 orifices of 0.005 m ID, are shown in Figure 2; and other details of this SBCR can be found elsewhere.[18,20]

Table 5. Correlations for Predicting the Physicochemical Properties of the Reactor Wax

$$\rho_L = 978.05 - 0.5403\,T \quad (15)$$

$$\mu_L = \exp\left(\frac{2504.2}{T} - 4.3371\right) \quad (16)$$

$$\sigma_L = \frac{1.367\ 10^{-4}T^2 - 0.1915\ T + 80.486}{1000} \quad (17)$$

$$\log_{10}(P_V) = -\frac{50951}{T^2} - \frac{1694.1}{T} + 3.146 \quad (18)$$

Experimental Hydrodynamic and Mass-Transfer Parameters

The hydrodynamic and mass-transfer parameters were measured for N_2 and various He/N_2 gaseous mixtures in the molten reactor wax in the pilot-scale SBCR shown in Figure 2, under different operating conditions typical to those of the LTFT process: P (4–31 bar), T (380–500 K), U_G (0.1–0.3 m/s), and C_S (0–45 wt %). The Transient Physical Gas Absorption technique was used to obtain the overall volumetric liquid-side mass-transfer coefficients of the gases in the liquid phase or slurry phase. The manometric method, also known as the hydrostatic head method, was followed to obtain the total gas holdup. Also, the Dynamic Gas Disengagement (DGD) technique was used to obtain the bubble-size distribution and the Sauter-mean bubble diameters. The experimental procedures followed were similar to those detailed in our previous publications.[18,20,30] The k_La, ε_G, and d_{32} values were also calculated using Eqs. 19 through 21 given in Table 6.

Gas holdup

The gas holdup values for N_2 and He/N_2 gas mixtures in the molten reactor wax appeared to generally decrease with increasing the solid concentration under the operating conditions shown in Figure 3. This behavior was due to the increase of the slurry viscosity and density, which resulted in low gas momentum per mass of slurry and large gas bubbles as shown in Figure 4. This behavior is in agreement with previous findings by Vandu et al.[16] using alumina particles in a C_9–C_{11} paraffins mixture; Deckwer et al.[8] using alumina particles in paraffin wax; Bukur et al.,[9–12] Daly et al.,[13] and Patel et al.[14] using iron oxide and silica particles in FT-300 wax and Sasol wax; Krishna et al.[15] using silica particles in paraffins oil; Behkish et al.[18] using alumina particles in isoparaffins mixture (Isopar-M); and Sehabiague and Morsi[20] using alumina and iron oxide particles in C_{12}–C_{13} paraffins mixture and FT cuts. In the absence and presence of solid particles up to 45 wt %, the gas holdup values for N_2 in the molten reactor wax appear to increase with temperature as depicted in Figure 3, which is in accord with other literature data.[10,18,20] This behavior was attributed to the decrease of the liquid-phase viscosity and surface tension with increasing temperature which led to the high gas holdup values.

Moreover, the gas holdup values were found to increase with reactor pressure, which is in agreement with other reported findings.[18,20,30] This behavior was due to the increase of the gas density and consequently the gas-phase momentum, which led to the increase of the gas holdup. Similarly, the gas holdup of N_2 in the molten reactor wax appeared to increase with the superficial gas velocity due to the increase of the gas momentum.

The gas holdup values were also found to increase with increasing the mole fraction of N_2 or decreasing the mole faction of He in the gas mixture, which is in agreement with earlier findings for He, N_2 and He/N_2 mixtures in an isoparaffinic mixture (Isopar-M), and in three different F-T liquids.[18,20] The presence of the heavier gas (N_2) increases the density and thus the momentum of the gaseous mixture, leading to the increase of the gas holdup and to the formation of small gas bubbles,

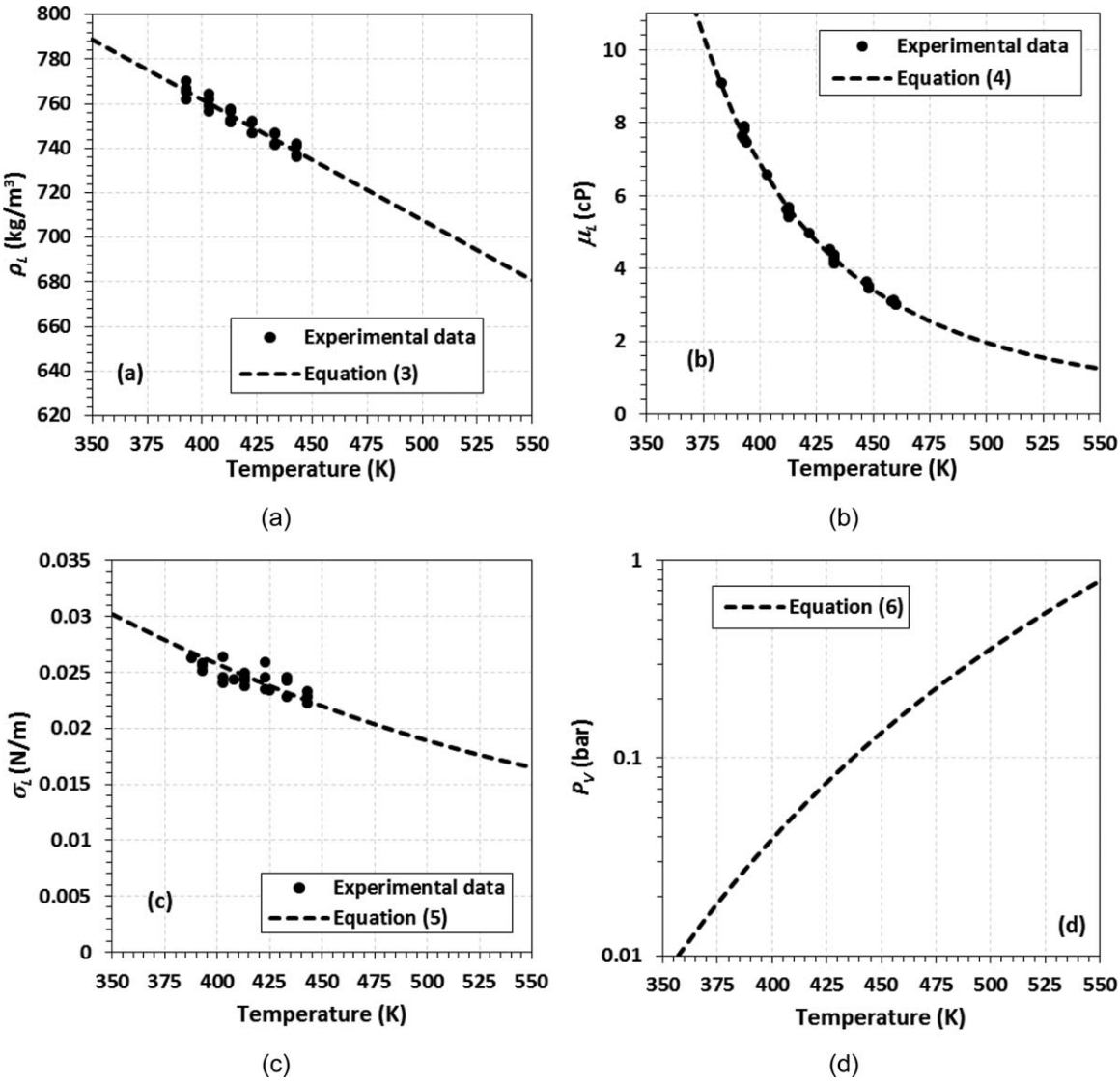

Figure 1. Effect of temperature on the density (a), viscosity (b), surface tension (c), and vapor pressure (d) of the molten reactor wax.

resulting in a greater gas-liquid interfacial area and consequently k_La. Indeed, k_La values increased with increasing the mole fraction of N_2 in the gaseous mixture, with the highest k_La data observed for N_2 as a single component.

Sauter mean bubble diameter

The Sauter-mean diameter of gas bubbles increased with increasing the concentration of solid particles under the operating conditions used as shown in Figure 4, which is in agreement with other findings.[18,20] This behavior is due to the increase of slurry viscosity with solid concentrations, which increases the bubbles coalescence, leading to the formation of large gas bubbles and consequently large Sauter mean bubble diameters. In the presence of solid particles up to 45 wt %, the superficial gas velocity appeared to have insignificant effect on the Sauter-mean gas bubble diameter for N_2 in the reactor wax, indicating that the addition of solid particles prevented the gas bubbles breakup. Figure 4 also shows that in the absence and presence of solid particles up to 34 wt %, the values of the Sauter mean bubble diameters decrease with increasing temperature, which can be attributed to the decrease of the liquid viscosity and surface tension with increasing temperature, leading to the formation of small gas bubbles.[18] Figure 5 underscores this behavior since increasing temperature from 390 to 450 K appears to shift the gas bubbles distribution toward small gas bubbles <3 mm. Figure 4 also shows that a minimum Sauter mean bubble diameter of about 0.2 mm is reached for solid concentrations up to 20 wt % and that at the highest solid concentration of 45 wt %, the temperature has negligible effect on the gas bubbles size.

Volumetric mass-transfer coefficients

Figure 6 shows that in the presence of solid particles, the volumetric mass-transfer coefficients values for N_2 and He/N_2 mixtures in molten wax increase with increasing temperature. In the absence of solid particles, the k_La values appear to level off after 440 K where the minimum Sauter mean bubble diameter was reached (see Figure 4). Also, at similar temperatures, k_La values for the same gas-liquid system decrease with increasing solid concentration, which is in agreement with other findings.[19,20] This behavior can be related the decrease of the gas holdup and the increase of the Sauter mean bubble diameter with increasing solid concentration as shown in Figures 3 and 4.

Figure 2. Photographs of the SBCR (left) and gas distributor (right).

[Color figure can be viewed in the online issue, which is available at wileyonlinelibrary.com.]

The k_La for N_2 in the molten reactor wax, with and without solid particles, also appeared to increase with increasing pressure, which was due to the increase of the gas holdup and the decrease of the Sauter mean gas bubble diameter, leading to the increase of the gas-liquid interfacial area. Moreover, as expected, k_La for N_2 in the molten reactor wax always increased with increasing the superficial gas velocity, which was attributed to the increase of the gas holdup and turbulences, which increased the gas-liquid interfacial area (a) and the mass-transfer coefficient (k_L), respectively.

Comparison with data obtained in a light FT cut

The hydrodynamic and mass-transfer data obtained in this study for the gases in the molten reactor wax were compared with those reported for a light FT cut under similar operating conditions using the same experimental setup.[20] The comparison showed that the data obtained with each liquid were obviously different, even though, both liquids are paraffinic waxes obtained from FT synthesis. For instance, in the absence and presence of solid particles, at temperatures >440 K, the gas holdup values obtained with the reactor wax were consistently greater than those in the light FT cut, although under similar conditions the viscosity and surface tension and even the vapor pressure of the reactor wax were always greater than those of the light FT cut. This behavior could be related to the fact that the reactor wax was produced using an iron-based catalyst and as such it could contain more alkenes and oxygenates,[31] such as alcohols, carbonyls and carboxylic acids than those in the light FT cut, which was produced using a cobalt-based catalyst. The presence of these alkenes and oxygenates could have led to the formation of smaller gas bubbles, which increased the gas holdup.

Table 6. Equations for Calculating the Hydrodynamic and Mass-Transfer Parameters

$$\frac{dC_L}{dt} = k_L a(C* - C_L) \tag{19}$$

$$\varepsilon_G = \frac{c_S\rho_S + (1-c_S)\rho_L}{c_S\rho_S + (1-c_S)\rho_L - \rho_G}\left(1 - \frac{\Delta P_{cell}}{(c_S\rho_S + (1-c_S)\rho_L)g\Delta H_{cell}}\right) \tag{20}$$

$$d_{32} = \frac{\sum_i n_i d_{b,i}^3}{\sum_i n_i d_{b,i}^2};\quad d_{b,i} = \frac{U_{b,i}^2}{1.69g};\quad U_{b,i} = \frac{\Delta H_{cell}}{t} \tag{21}$$

Also, despite the fact that the behaviors of the Sauter mean bubble diameter in both waxes were similar, the minimum Sauter mean bubble diameter in the reactor wax, shown in Figure 4, was about 0.2 mm, which is 50% smaller than that obtained in the light FT cut (0.4 mm). This behavior is surprising since the viscosity of the molten reactor wax is greater than that of the light FT cut, and the Sauter mean bubble diameter is expected to increase with the liquid viscosity.[18] Again, this is most likely related to the presence of alkenes and oxygenates in the molten reactor wax.

Furthermore, the k_La values measured for N_2 in the molten reactor wax were smaller than those reported for N_2 in the light FT cut, even though at temperatures above 440 K the gas-liquid interfacial area in the reactor wax should be greater than that in the light FT cut due to the greater gas holdup and smaller Sauter mean bubble diameters of N_2 in the reactor wax than those reported in the light F-T cut. This indicates that the liquid-side mass-transfer coefficient (k_L) of N_2 in the reactor wax is much smaller than that in the light FT cut, which can be related to its higher viscosity. It is known that the k_L of the gas is directly proportional to its diffusivity in the liquid to the power 0.5 or 1 according to the penetration theory or the two-film model, respectively. Therefore, at 500 K, the k_L of N_2 in the reactor wax would be 0.46–0.68 of that in the light FT cut according to the diffusivity equation by Wilke and Chang.[32]

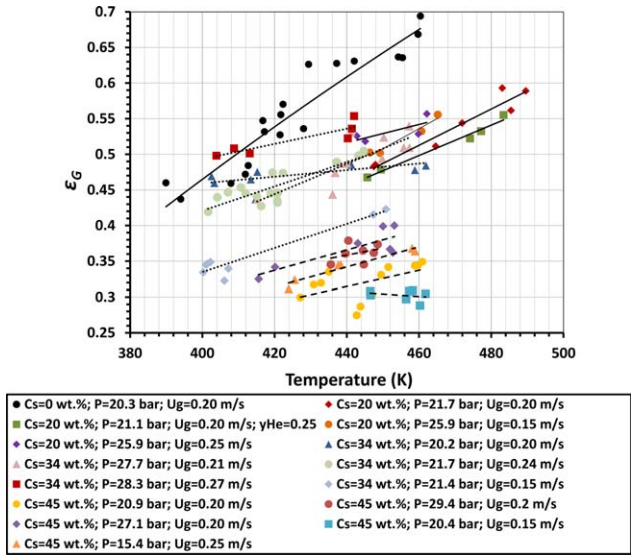

Figure 3. Effect of temperature and solid concentration on ε_G in reactor wax.

[Color figure can be viewed in the online issue, which is available at wileyonlinelibrary.com.]

Thus, it is imperative to develop hydrodynamic and mass-transfer correlations based on the data specifically obtained in the reactor wax produced with iron-based catalyst to adequately predict the performance of a large-scale SBCR operating with this same catalyst.

Comparison with published gas holdup and Sauter bubble diameter data in SBCRs

Figure 7 shows a comparison between our gas holdup data and available experimental values obtained by numerous investigators under different operating conditions as given in Table 7. As can be observed, the gas holdup data obtained in this work are notably greater than all other data depicted in the figure. This behavior can be attributed to the high pressure values used in this work (15.6 and 20.5 bar), which increased the gas density, momentum, and thus the gas holdup.[34] This behavior is further supported by that of data sets 5 and 6 obtained at lower pressures of 11.7 and 7.5 bar by Behkish et al.[18,19] Also the relatively high gas holdup (data set 8) by Deckwer et al.[8] obtained at 8 bar and 523 K were measured at low gas velocities (0.005–0.03 m/s) and no direct comparison with our data can be made.

The gas holdup data by Bukur et al.[9–12] (data set 9) obtained at ambient pressure (1 bar) and high temperature (538 K) in a 0.21 m ID column are greater than those (data set 7) by Behkish et al.[18,19] and those (data sets 13 and 14) by Krishna et al.[15] obtained at 1 bar and 298 K, respectively. This behavior was expected since increasing temperature decreases the liquid properties (viscosity, surface tension, and density), which enhance the gas bubbles breakup, leading to the formation of numerous small bubbles, thus increasing the gas

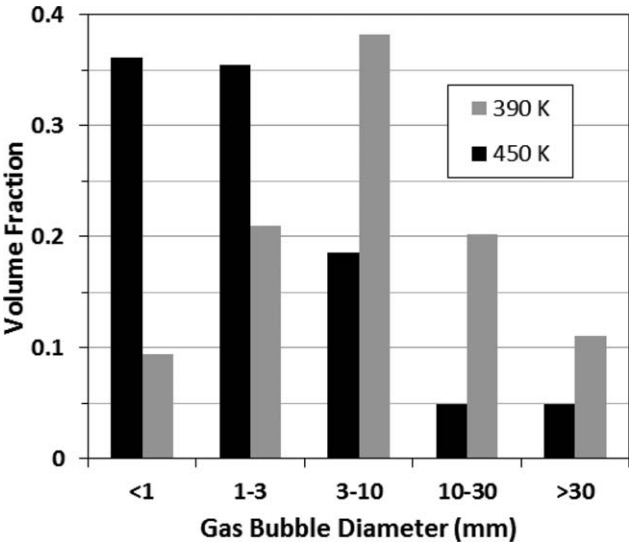

Figure 5. Effect of temperature on gas bubbles distribution (N_2, 21 bar, 0.2 m/s).

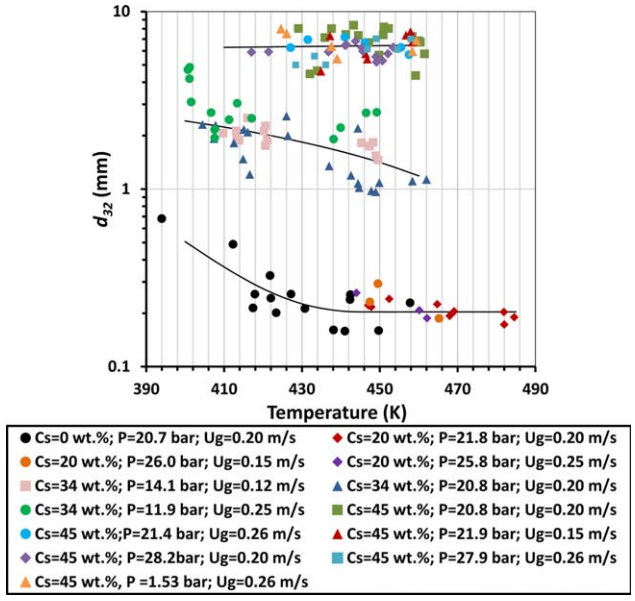

Figure 4. Effect of Temperature and Solid Concentration on d_{32} in reactor wax.

[Color figure can be viewed in the online issue, which is available at wileyonlinelibrary.com.]

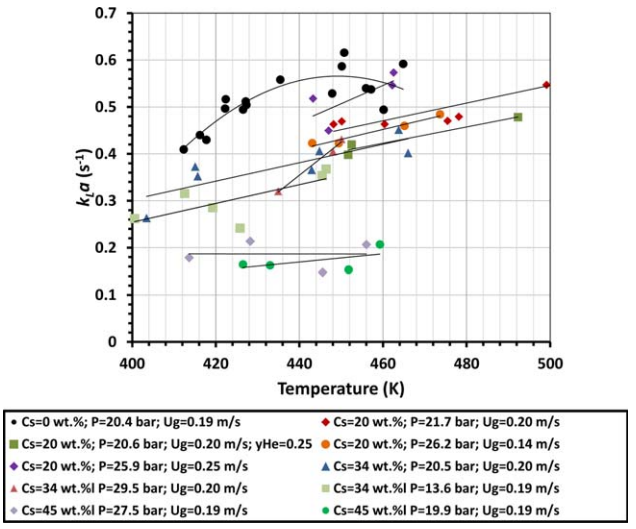

Figure 6. Effect of temperature and solid concentration on k_La in the reactor wax.

[Color figure can be viewed in the online issue, which is available at wileyonlinelibrary.com.]

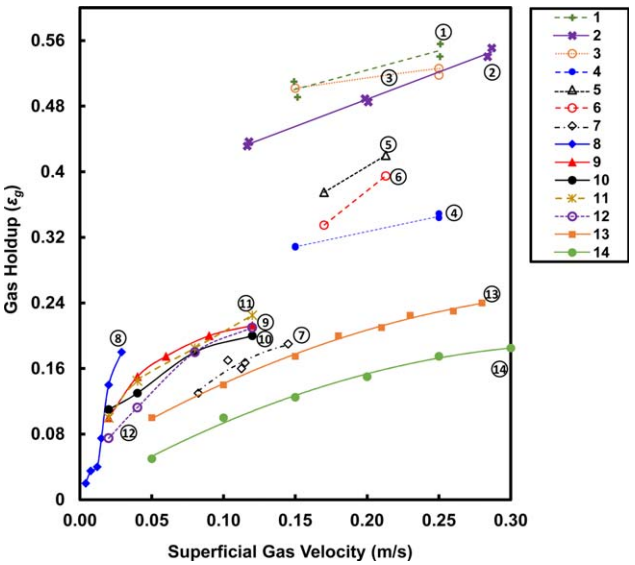

Figure 7. Comparison between our gas holdup data and experimental literature values.

[Color figure can be viewed in the online issue, which is available at wileyonlinelibrary.com.]

holdup. As a matter of fact, under 1 bar, Bukur et al.[9–12] reported small bubble diameters between 0.9 and 1.4 mm at 538 K, whereas Behkish et al.[18,19] reported bubble diameters between 2 and 3 mm at 400 K. Conversely, increasing temperature decreases the gas density and its momentum, thus decreasing the gas holdup. It appears that the effect of decreasing liquid properties on the gas holdup was more significant than that of decreasing the gas momentum, since the gas holdup was found to increase with temperature.

Figure 8 shows a comparison between our Sauter mean bubble diameter (d_{32}) and experimental values obtained by Patel et al.[14,33] and Bukur et al.[9–12,33] under different conditions as given in Table 8. It should be emphasized that their data were measured under ambient pressure (1 bar) and high temperature (538 K) in different waxes using the DGD technique in the absence of solid particles. As can be observed in this figure, our (d_{32}) values (data sets 1–6) vary between 0.18 and 6 mm; and the values (data set 7) by Patel et al.[14,33] and (data set 8) by Bukur et al.[9–12,33] measured in a 0.23 and 0.21 m diameter columns, respectively, at gas velocities (<0.12 m/s) were between 0.27 and 1.7 mm. As mentioned above, increasing temperature enhances gas bubbles breakup, leading to the formation of numerous small bubbles; and increasing pressure shrinks further these gas bubbles, leading to small values of d_{32}. Conversely, increasing solid concentration, increases the slurry viscosity thereby increasing the bubble coalescence and the formation of large bubbles, resulting in high values of d_{32}. Thus, these two opposing effects should dictate the resultant value of the Sauter mean bubble diameter. Based only on the temperature, our d_{32} values were supposed to be greater than those by Patel et al.[14,33] and Bukur et al.[9–12,33] since our temperature is lower. Also, based on the presence of solids in addition to the higher viscosity of the reactor wax used in this work, our d_{32} was supposed to be greater than those by those authors. However, the much greater pressure used in this work appeared to suppress the bubble growth and reduce the bubble size, leading to d_{32} in the range of from 0.18 to 6 mm, which is in agreement with previous findings.[35]

Table 7. Experimental Gas Holdup Data used in Figure 7

		Operating Conditions			Reactor Dimensions			Liquid			Solid			Gas
#	References	T (K)	P (bar)	C_v(wt %)	D_c(m)	H_c (m)	Gas Distributor, d_o (mm)	Type	ρ_L (kg/m^3)	μ_L (mPa·s)	σ_L (Nm^{-1})	Type	ρ_s (kg/m^3)	d_p (μm)	N_2
1	This work	461	15.6	20	0.29	3	Spider, 5	Reactor Wax	728.97	2.989	0.0213	Fe-based	3380	81	N_2
2	This work	443	20.5	34	0.29	3	Spider, 5	Reactor Wax	738.70	3.727	0.0225	Fe-based	3380	81	N_2
3	This work	445.9	25.9	20	0.29	3	Spider, 5	Reactor Wax	737.13	3.593	0.0223	Fe-based	3380	81	N_2
4	This work	459.5	20.7	45	0.29	3	Spider, 5	Reactor Wax	729.78	3.043	0.0214	Fe-based	3380	81	N_2
5	Behkish et al.[18,19]	400	11.7	32.8	0.29	3	Spider, 5	Isopar-M	733.21	0.909	0.0213	Alumina powder	3218.3	42.4	N_2
6	Behkish et al.[18,19]	400	7.5	32.8	0.29	3	Spider, 5	Isopar-M	733.21	0.909	0.0213	Alumina powder	3218.3	42.4	N_2
7	Behkish et al.[18,19]	298	1.75	41.2	0.316	2.82	Spider, 5	Isopar-M	783.343	2.705	0.0277	Glass beads	2500	19	N_2
8	Deckwer et al.[8]	523	8	16	0.1	0.6–1[a]	Sintered plate, 0.075	Molten Paraffin	670	2.0	0.021	Alumina powder	1284	≤5	N_2
9	Bukur et al.[9–12,33]	538	1	20	0.21	3	Perforated Plate, 2	Sasol Wax	655	2.0	0.016	Iron Oxide	5100	20–44	N_2
10	Bukur et al.[9–12,33]	538	1	20	0.21	3	Perforated Plate, 2	Sasol Wax	655	2.0	0.016	Iron Oxide	5100	0–5	N_2
11	Bukur et al.[9–12,33]	538	1	20	0.21	3	Perforated Plate, 2	Sasol Wax	655	2.0	0.016	Silica	2650	20–44	N_2
12	Bukur et al.[9–12,33]	538	1	20	0.21	3	Perforated Plate, 2	FT-300 Wax[b]	681	2.7	0.017	Iron Oxide	5100	20–44	N_2
13	Krishna et al.[15]	298	1	58.9	0.38	4	Sintered plate, 0.05	Paraffin Oil	790	2.9	0.028	Silica particles	2100	≤47	Air
14	Krishna et al.[15]	298	1	59.9	0.38	4	Sintered plate, 0.05	Paraffin Oil	790	2.9	0.028	Silica particles	2100	≤47	Air

[a]Suspension height.
[b]Liquid velocity = 0.005 m/s.

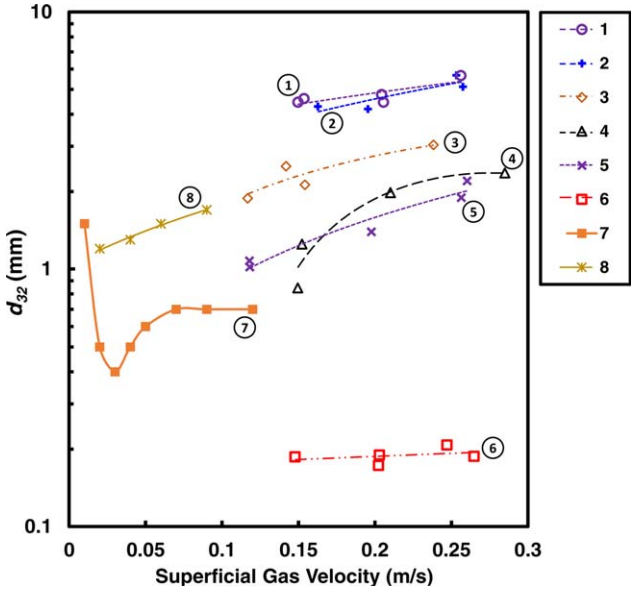

Figure 8. Comparison between our Sauter mean bubble diameter data and experimental literature values.

[Color figure can be viewed in the online issue, which is available at wileyonlinelibrary.com.]

Correlations for the hydrodynamics and mass-transfer parameters

Using the experimental data obtained in our pilot scale SBCR operating with the molten reactor wax, the following parameters required by the model described above can be estimated: (1) overall gas holdup; (2) large and small gas bubble holdups; (3) Sauter mean bubble diameters of large and small gas bubbles; and (4) gases volumetric gas-liquid mass-transfer coefficients. The hydrodynamics and mass-transfer data obtained in the reactor wax were compared with the predictions of different correlations available in the literature by calculating the average relative error (ARE), the absolute average relative error (AARE) and their associated standard deviations (SD).

Overall Gas Holdup Correlation. The overall gas holdup data were compared with the predictions of available literature correlations shown in Table 9. It should be noted that most of these correlations were developed for gas-liquid systems. Results of the comparisons are shown in Table 10; and as can be observed the correlation by Sehabiague and Morsi[20] gives the best prediction closely followed by that of Hammer et al.,[36] Joshi and coworkers,[37] Wilkinson et al.,[6] and Urseanu et al.[38] The correlation by Sehabiague and Morsi[20] was further modified as shown in Eq. 22 to enhance the accuracy of the gas holdup data predictions as given in Table 10 and Figure 9a

$$\varepsilon_G = 1.235\times10^4 \frac{\rho_g^{0.174} U_g^{0.553} \Gamma^{0.053}}{\rho_L^{1.59} \mu_L^{0.025} \sigma_L^{0.105}} \left(\frac{P}{P-P_v}\right)^{0.203} \left(\frac{1+D_C}{D_C}\right)^{0.117} \times \exp\left(-0.00015C_P - 1.78\times10^{-6}C_P^2 - 433.9d_P + 0.434X\right) \quad (22)$$

Sauter Mean Diameter of Gas Bubbles Correlation. The Sauter mean bubble diameter data presented in Figure 4 show that at temperatures above 440 K, the d_{32} values remain almost constant at 0.2 mm at various pressures and superficial gas velocities for low solid concentrations up to 20 wt % (This corresponds to a volumetric solid concentration of 5 vol %

Table 8. Experimental Sauter Mean Bubble Diameters used in Figure 8

		Operating Conditions			Reactor Dimensions			Liquid				Solid			Gas
#	References	T (K)	P (bar)	C_v(wt %)	D_c (m)	H_c(m)	Gas Distributor, d_o (mm)	Type	ρ_L (kg/m^3)	μ_L (mPa·s)	σ_L (Nm^{-1})	Type	ρ_s (kg/m^3)	d_p (μm)	N_2
1	This work	429.1	14.29	34	0.29	3	Spider, 5	Reactor Wax	746.21	4.476	0.0235	Fe-based	3380	81	N_2
2	This work	455.9	27.63	45	0.29	3	Spider, 5	Reactor Wax	731.73	3.176	0.0216	Fe-based	3380	81	N_2
3	This work	414	14.95	34	0.29	3	Spider, 5	Reactor Wax	754.37	5.538	0.0246	Fe-based	3380	81	N_2
4	This work	443	27.85	34	0.29	3	Spider, 5	Reactor Wax	738.69	3.727	0.0225	Fe-based	3380	81	N_2
5	This work	444.3	21.07	34	0.29	3	Spider, 5	Reactor Wax	733.21	3.666	0.0224	Fe-based	3380	81	N_2
6	This work	470.8	24.66	20	0.29	3	Spider, 5	Reactor Wax	723.68	2.669	0.0206	Fe-based	3380	81	N_2
7	Patel et al.[14,33]	538	1	0	0.23	3	Perforated Plate, 2	FT-300 Wax	681	2.7	0.017	–	–	–	N_2
8	Bukur et al.[9–12,33]	538	1	0	0.21	3	Perforated Plate, 2	Sasol Wax	655	2.0	0.016	–	–	–	N_2

Table 9. Literature Correlations of the Overall Gas Holdup in BCRs and SBCRs

References	Correlation	
Akita and Yoshida[39]	$\frac{\varepsilon_G}{(1-\varepsilon_G)^4}=0.2\left(\frac{gD_C^2\rho_L}{\sigma_L}\right)^{0.125}\left(\frac{gD_C^3}{\mu_L}\right)^{0.083}\left(\frac{U_G}{\sqrt{gD_C}}\right)$	(23)
Koide et al.[40]	$\frac{\varepsilon_G}{(1-\varepsilon_G)^4}=0.277\left(\frac{U_G\mu_L}{\sigma_L}\right)^{0.918}\left(\frac{g\mu_L^4}{\rho_L\sigma_L^3}\right)^{-0.252}$	(24)
Hammer et al. (1984) as reported in[36]	$\frac{\varepsilon_G}{1-\varepsilon_G}=0.4\left(\frac{U_G\mu_L}{\sigma_L}\right)^{0.87}\left(\frac{\mu_L^4 g}{\rho_L\sigma_L^3}\right)^{-0.27}\left(\frac{\rho_G}{\rho_L}\right)^{0.17}$	(25)
Reilly et al.[41]	$\varepsilon_G=296U_G^{0.44}\rho_L^{-0.98}\sigma_L^{-0.16}\rho_G^{0.19}+0.009$	(26)
Dharwadkar et al.[42]	$\varepsilon_G=0.07U_G^{0.5}\mu_L^{-0.04}\sigma_L^{-0.75}$	(27)
Bukur et al.[10]	$\varepsilon_g=0.24\left(\left(\frac{U_G^2}{dD_c}\right)^{0.28}\left(\frac{D_c^2\rho_{sl}g}{\sigma_L}\right)^{0.14}\right)$ where: $\rho_{sl}=\frac{1}{\left(\frac{C_s}{\rho_s}+\frac{(1-C_s)}{\rho_L}\right)}$	(28)
Wilkinson et al.[6]	$U_G<U_{trans}\quad \varepsilon_G=\frac{U_G}{U_{s,b}}$; $U_G>U_{trans}\quad \varepsilon_G=\left(\frac{U_{trans}}{U_{s,b}}\right)+\frac{U_G-U_{trans}}{U_{l,b}}$; $\frac{U_{trans}}{U_{s,b}}=0.5\exp\left(-193\rho_G^{-0.61}\mu_L^{0.5}\sigma_L^{0.11}\right)$; $\frac{\mu_L U_{l,b}}{\sigma_L}=\frac{\mu_L U_{s,b}}{\sigma_L}+2.4\mu_L\left(\frac{U_G-U_{trans}}{\sigma_L}\right)^{0.757}\left(\frac{\sigma_L^3\rho_L}{g\mu_L^4}\right)^{-0.077}\left(\frac{\rho_L}{\rho_G}\right)^{0.077}$; $\frac{\mu_L U_{s,b}}{\sigma_L}=2.25\left(\frac{\sigma_L^3\rho_L}{g\mu_L^4}\right)^{-0.273}\left(\frac{\rho_L}{\rho_G}\right)^{0.077}$	(29)
Joshi et al. (1998) as reported in[37]	$\varepsilon_G=0.62U_G^{0.56}\left(\frac{\sigma_w}{\sigma_L}\right)^{0.15}\left(\frac{\mu_w}{\mu_L}\right)^{0.15}\left(\frac{\rho_G}{\rho_a}\right)^{0.15}\left(\frac{\rho_w}{\rho_L}\right)^{0.15}$	(30)
Krishna et al.[43–45,50]	$\varepsilon_G=\varepsilon_{LB}+\varepsilon_{df}(1-\varepsilon_b)$; $\varepsilon_{LB}=\frac{(U_G-U_{df})}{V_{LB}}$; $U_{df}=V_{small}\varepsilon_{df}$; $V_{LB}=0.71\sqrt{gd_{LB}}(SF)(AF)(DF)$; $d_{LB}=0.069(U_G-U_{df})^{0.376}$; $SF=\begin{cases}1 & \frac{d_{LB}}{D_C}<0.125\\ 1.13\exp\left(-\frac{d_{LB}}{D_C}\right) & 0.125<\frac{d_{LB}}{D_C}<0.6\\ 0.496\sqrt{\frac{D_C}{d_{LB}}} & \frac{d_{LB}}{D_C}>0.6\end{cases}$; $AF=2.25+4.09(U_G-U_{df})$; $DF=\sqrt{\frac{1.29}{\rho_G}}$; $V_{small}=V_{small,0}\left(1+\frac{0.8}{V_{small,0}}C_S\right)$; $V_{small,0}=\frac{1}{2.84}\frac{\sigma_L^{0.12}}{\rho_G^{0.04}}$; $\varepsilon_{df}=\varepsilon_{df,0}\left(1-\frac{0.7}{\varepsilon_{df,0}}C_S\right)$; $\varepsilon_{df,0}=0.59B^{1.5}\sqrt{\frac{\rho_G^{0.96}\sigma_L^{0.12}}{\rho_L}}$; $B=3.85$	(31)

TABLE 9. *Continued*

References	Correlation	
Urseanu et al.[38] (valid for viscous liquids 0.05–0.55 Pa.s)	$\varepsilon_G = 0.21 U_G^{0.58} D_C^{-0.18} \mu_L^{-0.12} \rho_G^{0.3\exp(-9\mu_L)}$	(32)
Gandhi et al.[37]	Support vector regression (SVR)-based correlation	(33)
Nedeltchev and Schumpe[51]	$\varepsilon_G = f_c \frac{d_{32} f_B S_B}{6 A U_B}$ $U_B = \sqrt{\frac{2\sigma_L}{\rho_L d_e} + \frac{g d_e}{2}}; \quad S_B = \pi \frac{l^2}{2}\left[1 + \left(\frac{h}{l}\right)^2 \frac{1}{2e} \ln \frac{(1+e)}{(1-e)}\right]; \quad V_B = \frac{\pi d_e^3}{6}$ $e = \sqrt{1 - \left(\frac{h}{l}\right)^2}; \quad d_e = (l^2 h)^{1/3}$ $f_c = 0.78 \left(\frac{g(\rho_L - \rho_G) d_e^2}{\sigma_L}\right)^{-0.22} \left(\frac{\rho_G}{\rho_{G-ref}}\right)^{0.07}; \quad f_B = \frac{Q_G}{V_B}$ $2 < \mathrm{Ta} < 6: \begin{cases} l = \frac{d_e}{1.14 \mathrm{Ta}^{-0.176}} \\ h = 1.3 d_e \mathrm{Ta}^{-0.352} \end{cases}; \quad 6 < \mathrm{Ta} < 16.5: \begin{cases} l = \frac{d_e}{1.36 \mathrm{Ta}^{-0.28}} \\ h = 1.85 d_e \mathrm{Ta}^{-0.56} \end{cases}$ $\mathrm{Ta} = \mathrm{Re}_B \mathrm{Mo}^{0.23}; \quad \mathrm{Re}_B = \frac{d_e U_B \rho_L}{\mu_L}; \quad \mathrm{Mo} = \frac{g \mu_L^4}{\rho_L \sigma_L^3}$	(34)
Sehabiague and Morsi[20]	$\varepsilon_G = 11241.6 \frac{\rho_g^{0.174} U_g^{0.553} \Gamma^{0.053}}{\rho_L^{1.59} \mu_L^{0.025} \sigma_L^{0.105}} \left(\frac{P}{P - P_v}\right)^{0.203} \left(\frac{1 + D_C}{D_C}\right)^{0.117}$ $\times \exp\left(-0.0012 C_P - 4\times10^{-7} C_P^2 - 433.9 d_P + 0.434 X\right)$	(35)

based on the skeletal density of solid particles). Also, d_{32} values greatly increase with increasing the solid concentration up to 45 wt %. As shown in Tables 11 and 12, the correlations by Fukuma et al.[46] and Wilkinson et al.,[47] which were developed for gas-liquid systems, were unable to predict the experimental data in the presence of solids which was not surprising. Similarly, the correlation by Lemoine and Morsi.[48] could not predict the data with acceptable accuracy. Therefore, a more accurate correlation, similar to that of Lemoine and Morsi,[48] was developed to predict the gas Sauter mean bubble diameter for catalyst volumetric concentrations less or greater than 5 vol % as shown in Eq. 36

$$\text{if } C_V < 5 \text{ vol.\%} \quad d_{32} = 0.213 e^{2.81 C_V} F$$
$$\text{if } C_V \geq 5 \text{ vol.\%} \quad d_{32} = 0.0574 e^{29 C_V} F$$
$$F = \frac{\mu_L^{0.08} \sigma_L^{1.22} \rho_g^{0.02} T^{1.66} U_g^{0.14}}{\rho_L^{1.52} M_{W_g}^{0.12}} \left(\frac{D_C}{D_C + 1}\right)^{0.3} \left(1 - \varepsilon_g\right)^{1.56} \Gamma^{-0.02} \tag{36}$$

Table 10. Comparison among Perditions of the Gas Holdup Correlations

References	ARE	SD (ARE)	AARE	SD(AARE)
This study: Eq. 22	−0.9%	9.5%	7.3%	6.1%
Sehabiague and Morsi[20]	−17.9%	10.1%	18.9%	8.1%
Hammer et al. (1984) as reported in[36]	−3.0%	20.4%	17.9%	10.2%
Bukur et al. (1990)[10]	−20.93%	18.3%	23.32%	15.1%
Joshi et al. (1998) as reported in[37]	−9.9%	18.9%	18.9%	9.9%
Wilkinson et al.[6]	−13.9%	18.5%	20.7%	10.3%
Urseanu et al.[38]	6.5%	22.9%	19.1%	14.2%
Krishna et al.[43–45,50]	23.6%	19.0%	25.5%	16.4%
Koide et al.[40]	−56.4%	7.3%	56.4%	7.3%
Gandhi et al.[37]	−53.7%	11.6%	53.7%	11.6%
Dharwadkar et al.[42]	66.2%	35.9%	66.2%	35.8%
Reilly et al.[41]	71.8%	35.4%	71.8%	35.4%
Akita and Yoshida[39]	>100%	>100%	79.3%	4.7%
Nedeltchev and Schumpe[51]	85.8%	47.6%	85.9%	47.5%

Holdup of Large Gas Bubbles Correlation. The data for the holdup of large gas bubbles were compared with the correlations by Behkish et al.[49] and by Krishna et al. [43–45,50] as shown in Table 13; and due to its superior accuracy (see Table 14), it was decided to include the correlation by Behkish et al.[49] in the reactor model.

Diameter of Large Gas Bubbles Correlation. As shown in Tables 15 and 16, the correlation by Krishna et al.[45] proposed for gas-liquid systems could not predict the size of the large gas bubbles, whereas that by Lemoine and Morsi[52] under-predicted the size of large gas bubbles by an average of 93%. The latter correlation was then modified as shown in Eq. 41 to predict the experimental data with better accuracy as shown in Table 16

$$d_{LB} = d_{32}^{0.78} \left(1 - 10^{-5} \rho_L^{0.22} \mu_L^{0.03} \sigma_L^{8.6} U_g^{0.04} \varepsilon_G^{2.37} \varepsilon_{LB}^{2.74}\right) \tag{41}$$

Volumetric Mass-Transfer Coefficient Correlation. The experimental $k_L a$ data obtained in this study were compared with the predictions of different literature correlations shown in

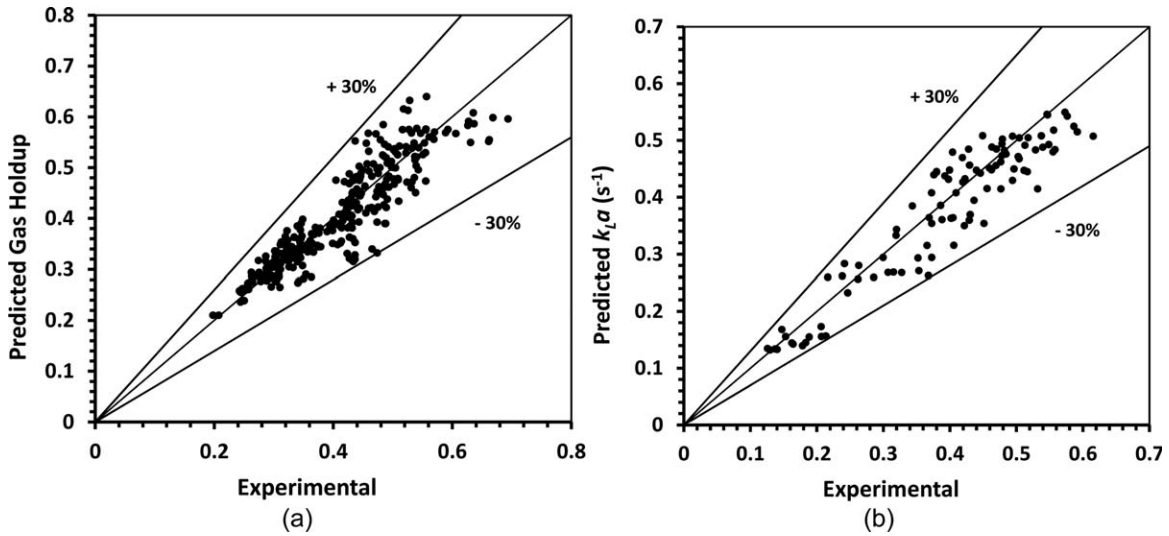

Figure 9. Comparison between experimental data and predicted values: (a) gas holdup using Eq. 22; (b) k_La using Eq. 35.

Table 11. Literature Correlations of the Gas Bubbles Sauter Mean Diameter

References	Correlation	
Fukuma et al.[46]	$d_{32}=\frac{0.59}{g}\left(\frac{V_D}{\bar{\varepsilon}_g}\right)^2;\quad V_D=U_g(1-\bar{\varepsilon}_g)-U_l\bar{\varepsilon}_g\frac{(1-\bar{\varepsilon}_g)}{\bar{\varepsilon}_l}$	(37)
Wilkinson et al.[47]	$d_{32}=3g^{-0.44}\sigma_L^{0.34}\mu_L^{0.22}\rho_L^{-0.45}\rho_G^{-0.11}U_G^{-0.02}$	(38)
Lemoine et al.[48]	$d_{32}=37.19\times\frac{\mu_L^{0.08}\sigma_L^{1.22}\rho_G^{0.02}T^{1.66}}{\rho_L^{1.52}M_{W\text{-}Gas}^{0.12}}\,U_G^{0.14}\left(\frac{D_C}{D_C+1}\right)^{0.30}(1-\varepsilon_G)^{1.56}\Gamma^{-0.02}\times\exp(-2.29X_W+2.81C_V+2.77\rho_P d_P)$	(39)

Table 12. Comparison among Predictions of the Gas Bubbles Sauter Mean Diameter Correlations

References	ARE	SD(ARE)	AARE	SD(AARE)
Equation 36	−34.9%	22.2%	37.4%	17.7%
Lemoine et al.[48]	>100%	>100%	>100%	>100%
Fukuma et al.[46]	>100%	>100%	>100%	>100%
Wilkinson et al.[47]	>100%	>100%	>100%	>100%

Table 13. Literature Correlations of the Large Gas Bubbles Holdup

References	Correlation	
Krishna et al.[43–45,50]	See Eq. 31	
Behkish et al.[49]	$\varepsilon_{LB}=\varepsilon_G^{0.84}\left(1-3.04\times10^{-6}\frac{\rho_L^{0.97}}{\mu_L^{0.16}}e^{4.5X_w-4.49C_v}\right)$	(40)

Table 14. Comparison among Predictions of the Large Gas Bubbles Holdup Correlations

References	ARE	SD (ARE)	AARE	SD(AARE)
Behkish et al.[49]	3.0%	24.8%	15.1%	19.9%
Krishna et al.[43–45,50]	−41.9%	24.5%	42.6%	23.3%

Table 15. Literature Correlations of the Large Gas Bubble Diameter

References	Correlation	
Krishna et al.[45]	$d_{LB}=0.069(U_G-U_{trans})^{0.376}$	(42)
Lemoine et al.[52]	$d_{LB}=d_{32}^{0.96}\left(1-10^{-5}\rho_L^{0.22}\mu_L^{0.03}\sigma_L^{8.60}U_G^{0.04}\varepsilon_G^{2.37}\varepsilon_{LB}^{2.74}\right)$	(43)

Table 16. Comparison among Predictions of the Large Gas Bubble Diameter Correlations

References	ARE	SD (ARE)	AARE	SD(AARE)
Equation 41	0.0%	51.9%	44.2%	27.0%
Lemoine et al.[52]	−93.0%	5.8%	93.0%	5.8%
Krishna et al.[45]	>100%	>100%	>100%	>100%

Table 17; and as can be observed in Table 18, the best prediction was obtained using the correlation by Sehabiague and Morsi,[20] which could predict the experimental data with an ARE of −9.9%. This correlation was further modified to increase the prediction accuracy as show in Eq. 44 and Figure 9b

$$k_La=9.34\times10^{-9}\frac{\rho_L^{1.82}\rho_g^{0.27}U_g^{0.387}\Gamma^{0.173}}{M_g^{0.02}\mu_L^{0.25}\sigma_L^{0.976}}\left(\frac{P}{P-P_v}\right)^{0.242}\left(\frac{D_C}{0.3+D_C}\right)^{0.1}\times\exp\left(-8\times10^{-9}C_P^3-1.6\times10^{-6}C_P^2-0.8C_P+1675.7d_P+0.176X\right)\quad(44)$$

Reactor model parameters

Table 19 summarizes the hydrodynamic and mass-transfer parameters predictive equations used in the model. Table 20 shows the kinetic expressions for the FT and WGS reactions, developed specifically for the iron-based catalyst used in the ID SBCR.

Table 17. Literature Correlations of the Volumetric Mass-Transfer Coefficients (k_La)

References	Correlation	
Koide et al.[40]	$\frac{k_L a\sigma_L}{\rho_L D_L g} = \frac{2.11\left(\frac{\mu_L}{\rho_L D_L}\right)^{0.5}\left(\frac{g\mu_L^4}{\rho_L\sigma_L^3}\right)^{-0.159}\varepsilon_G^{1.18}}{1+1.47\times10^4 C_V^{0.612}\left(\frac{V_t}{\sqrt{gD_C}}\right)^{0.486}\left(\frac{D_C^2 g\rho_L}{\sigma_L}\right)^{-0.477}\left(\frac{D_C U_G\rho_L}{\mu_L}\right)^{-0.345}}$	(45)
Nedeltchev and Schumpe[51]	$k_L a = f_c\sqrt{\frac{4D_L R_{sf}}{\pi S_B}}\frac{f_B S_B}{A U_B}$ $R_{sf} = \pi\sqrt{\frac{l^2+h^2}{2} - \frac{(l-h)^2}{8}}U_B$ See Eq. 34 for description of other parameters	(46)
Sehabiague and Morsi[20]	$k_L a = 7.99\times10^{-9}\frac{\rho_L^{1.82}\rho_g^{0.27}U_g^{0.387}\Gamma^{0.173}}{M_g^{0.02}\mu_L^{0.25}\sigma_L^{0.976}}\left(\frac{P}{P-P_v}\right)^{0.242}\left(\frac{D_C}{0.3+D_C}\right)^{0.1}$ $\times\exp\left(-10^{-9}C_P^3+0.8\times10^{-6}C_P^2-1.3C_P+1675.7d_P+0.176X\right)$	(47)

The syngas composition and reactor geometries as well as the operating conditions used in the model are listed in Tables 21 and 22, respectively.

Modeling results

The product selectivities were estimated assuming that products with carbon number (n) less than 30 follow the superposition of 2 Anderson–Schulz–Flory (ASF) distributions,[53] while the composition of the reactor wax was used to estimate the selectivities of the products with carbon number greater than 30. It should be emphasized that the hydrocarbon product distribution in FT reactors is dependent on the pressure and temperature, hence these estimated product selectivities are specific to the iron catalyst and the operating conditions used in this study. In addition, literature data by Chang et al.[54] available for an iron-based catalyst, similar to the one used in this study, were used to develop the following correlations to predict the α-olefins to paraffins (alkanes) ratio

$$n < 5\ \ \mathrm{Rop}_n = -1.06n^2+7.18n-6.25$$
$$n \geq 5\ \ \mathrm{Rop}_n = -0.000115n^4+0.00804n^3-0.188n^2+1.4n+1.47 \quad (48)$$

Again, the use of Eq. 48 should be limited to the catalyst and operating conditions employed in its development since the FT products distribution strongly depends on the reaction pressure and temperature.

One of the main factors limiting the yield of a FT reactor is the catalyst deactivation. It should be emphasized that the deactivation of iron-based catalysts in the LTFT process is mainly due to the presence of the water produced by the FT reaction. Steynberg et al.[5] recommended that to avoid rapid deactivation of the iron catalyst by oxidation, the water partial pressure in the reactor should be maintained <3 bar. Also, de Klerk[31] suggested that the ratio $H_2O/(H_2+CO)$ should preferably be kept <0.15. Usually, the syngas composition and flow rate as well as the operating temperature and pressure will be selected to achieve the desired product selectivities. Once those are set, the only remaining adjustable operating

Table 18. Comparison among Predictions of k_La Correlations

References	ARE	SD (ARE)	AARE	SD(AARE)
Equation 44	0.0%	14.0%	11.1%	8.5%
Sehabiague and Morsi[20]	−9.9%	22.0%	20.7%	12.4%
Koide et al.[40]	−16.2%	27.4%	28.2%	14.6%
Nedeltchev and Schumpe[51]	>100%	>100%	>100%	>100%

Table 19. Selected Correlations for the Hydrodynamic and Mass-Transfer Parameters

Gas holdup	Equation 22
Large gas bubbles holdup	Behkish et al.[49]
Gas bubbles diameter	Equation 36
Large gas bubbles diameter	Equation 41
Volumetric mass-transfer coefficient	Equation 44

Table 20. FT Catalyst and Kinetics Used in the Modeling

Catalyst	Kinetic Rate Expressions	Parameters	Selectivity Model Parameters
Fe based catalyst	$r_{FT} = \frac{k_{FT}P_{CO}P_{H_2}}{P_{CO}+aP_{H_2O}+aP_{CO_2}}$ $r_{WGS} = \frac{k_{WGS}\left(P_{CO}P_{H_2O} - {}^{P_{H_2}P_{CO_2}}/_{K_P}\right)}{\left(P_{CO}+bP_{H_2O}+bP_{CO_2}\right)^2}$	$k_{FT} = 1.18\times10^{-7}$ $a = 5.9$ $k_{WGS} = 0.083$ $b = 1.9$ $K_P = 79.7$	$n<30$: $\alpha_1 = 0.625$ $\alpha_2 = 0.945$ $\zeta = 9.25$ $n>30$: Selectivities calculated from reactor wax composition

Table 21. Syngas Composition

Component	Mole Fraction
H_2	0.5247
CO	0.3446
CO_2	0.0002
N_2	0.1272
O_2	0.0027
CH_4	0.0003
H_2S	<0.02 mg/Nm^3

Table 22. The Industrial-Scale FT SBCR Geometry and Operating Conditions

Reactor	L, m	26–42
	Diameter, m	5.8
Sparger	Sparger coefficient, r	100
Cooling Pipes	Number	604
	Outside diameter, m	0.057–0.089
Operating Variables	H_2/CO in the feed	1.7
	T, K	528
	P, bar	28
	U_g, m/s	0.24
	U_L, m/s	0.00015
	C_S, wt %	4–30

conditions that will affect the water partial pressure in the reactor will be the reactor height and the catalyst concentration. Therefore, modeling was carried out to predict the effects of these two parameters on the water partial pressure, syngas conversion and C_{5+} products yield. In these runs, the average gas holdups over the reactor height varied from 44 to 53%; the height-average gas Sauter mean bubble diameters were between 0.24 and 1.3 mm; and k_La values for H_2 were between 0.53 and 0.62 s^{-1} and for CO were between 0.34 and 0.39 s^{-1}.

Figure 10 illustrates the effect of reactor length-to-diameter (L/D) ratios at various catalyst concentrations on the water partial pressure at the reactor outlet. As can be seen in this figure, increasing L/D ratio at a constant catalyst loading only

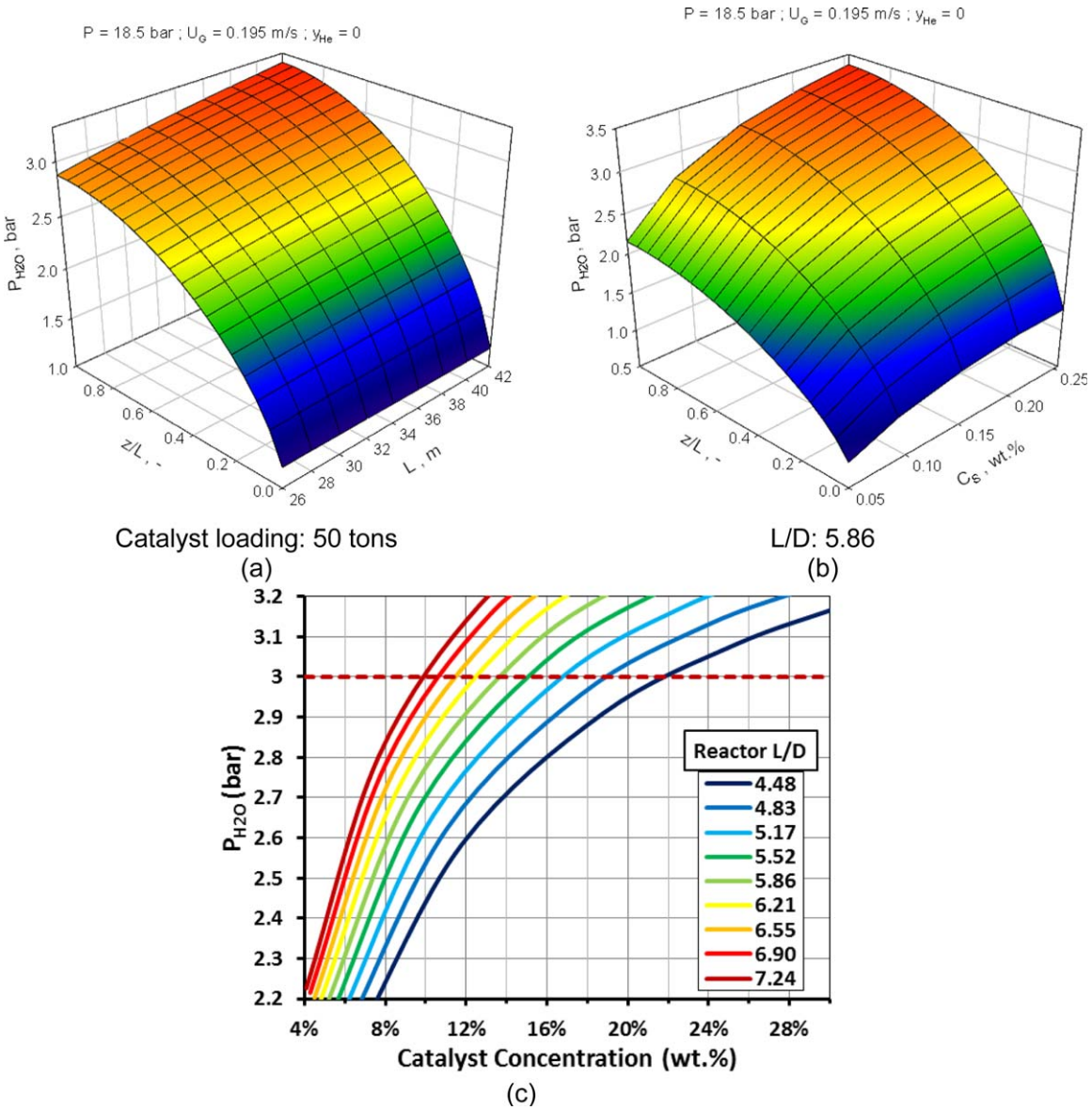

Figure 10. Effect of catalyst concentration and reactor height on water partial pressure.

[Color figure can be viewed in the online issue, which is available at wileyonlinelibrary.com.]

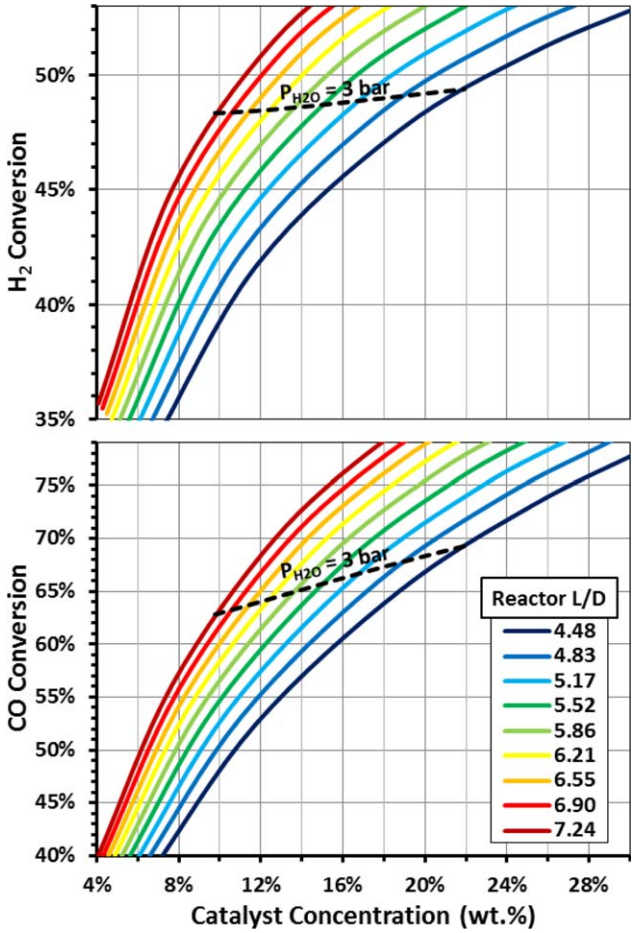

Figure 11. Effect of catalyst concentration and reactor height on syngas conversion.

[Color figure can be viewed in the online issue, which is available at wileyonlinelibrary.com.]

slightly increases the water partial pressure inside the reactor, while increasing catalyst concentration for a given reactor height significantly increases the water partial pressure. Therefore, the water partial pressure at the reactor outlet will be affected mostly by the total amount of catalyst in the reactor. As can be observed in Figure 10c, to maintain the water partial pressure < 3 bars at lower L/D values, higher catalyst loading can be used; and conversely, at higher L/D values, lower catalyst concentrations are possible. For instance, for $L/D = 4.48$, the catalyst concentration can be increased up to 22 wt %, while for $L/D = 7.24$, the catalyst concentrations should be maintained <10 wt %.

Figure 11 illustrates the effect of catalyst concentration on the H_2 and CO conversion at different reactor L/D; and as can be observed at a catalyst concentration of 22 wt % and a reactor L/D of 4.48, the H_2 and CO conversions are 49.4 and 69.3%, whereas at a catalyst concentration of 10 wt % and a reactor L/D of 7.24, the H_2 and CO conversions are 48.4 and 62.8%, respectively.

Considering the values of k_La obtained is >0.34 s^{-1} and the fact that no maximum was observed for H_2 and CO conversions presented in Figure 11, it can be concluded that over the range of operating conditions and catalyst concentrations used in the modeling, the SBCR is operating in the kinetically controlled regime, that is, the H_2 and CO conversions are directly limited by the slow FT and WGS reaction kinetics, while the mass transfer is fast enough and has insignificant effect on the syngas conversion. Also, Figure 11 indicates that despite the low H_2/CO ratio of 1.7 (<2) of the syngas feed to the reactor, H_2 conversion appears to be systematically lower than that of CO, which can be attributed to the high WGS activity of the iron-based catalyst. This also means that the H_2/CO ratio given in Table 22 is not optimal and higher syngas conversions could be achieved at lower H_2/CO ratios of the syngas feed. However, this would also have a significant impact on the product selectivities. According to the results of other studies[3,25,55] with iron-based FT catalysts, decreasing the H_2/CO ratio under 1.7 in the feed, would increase the selectivity of heavier products, such as wax.

The effects of reactor height and catalyst concentration on the concentration profiles of CO and H_2 in the different phases (liquid phase, pseudosmall bubbles-phase, and pseudo large bubbles-phase) were investigated. It should be mentioned that the concentration profiles for H_2 and CO were found to be qualitatively similar; and therefore only CO data are shown. Figures 12a, c, and e shows that at a given catalyst loading of 50 tons in the reactor, the concentration profiles of CO in the gaseous pseudophases slightly change, whereas those in the liquid phase become less uniform with increasing reactor height. For longer reactor height, the liquid-phase behavior approaches a plug flow and the CO concentration profile in the liquid phase becomes closer to that in the pseudo gaseous phases. Figures 12b, d, and f shows that at a constant L/D of 5.86, the concentration profiles of CO in the pseudo gaseous phases and the liquid phase are strongly affected by the catalyst concentration, and accordingly the catalyst concentration should have a stronger impact than the reactor height on the syngas conversion and C_{5+} products yield. These data confirm the behavior observed in Figures 10 and 11 and indicate that the ID SBCR used in this investigation is operating in the kinetically controlled regime under the conditions listed in Table 22.

Figures 13a and b indicates that the reactor height has almost no effect on the holdup of large gas bubbles, whereas it significantly affects the holdup of small gas bubbles, as greater and more uniform holdups are obtained at the tallest reactor. This behavior can be attributed to the lowest catalyst concentrations obtained at the tallest reactor for a constant catalyst loading of 50 tons. Figure 13c and d shows that the holdup of small gas bubbles greatly decrease with increasing catalyst concentration, while that of the large gas bubbles is slightly affected. This behavior was expected, since experimental studies[15,18] in SBCRs operating in the churn-turbulent flow regime revealed that increasing catalyst concentrations led to the disappearance of small gas bubbles, while large gas bubbles may or may not increase in size and population.

Figure 14 shows that maintaining the water partial pressure in the reactor under the recommended threshold of 3 bar, at a catalyst concentration of 22 wt % and a reactor L/D of 4.48, the C_{5+} products yield reaches 435.6 ton/day, while at a catalyst concentration of 10 wt % and a reactor L/D of 7.24, the C_{5+} products yield only reaches 412.7 ton/day. This is because the SBCR used in the modeling is operating in the kinetically controlled regime under the range of catalyst concentrations and L/D ratios listed in Table 22. Within such a regime, the effects of shorter syngas residence time (small L/D) and smaller mass-transfer coefficients (high solid concentrations) on the reactor performance were less important when compared with those of the reaction kinetics. Therefore, for the

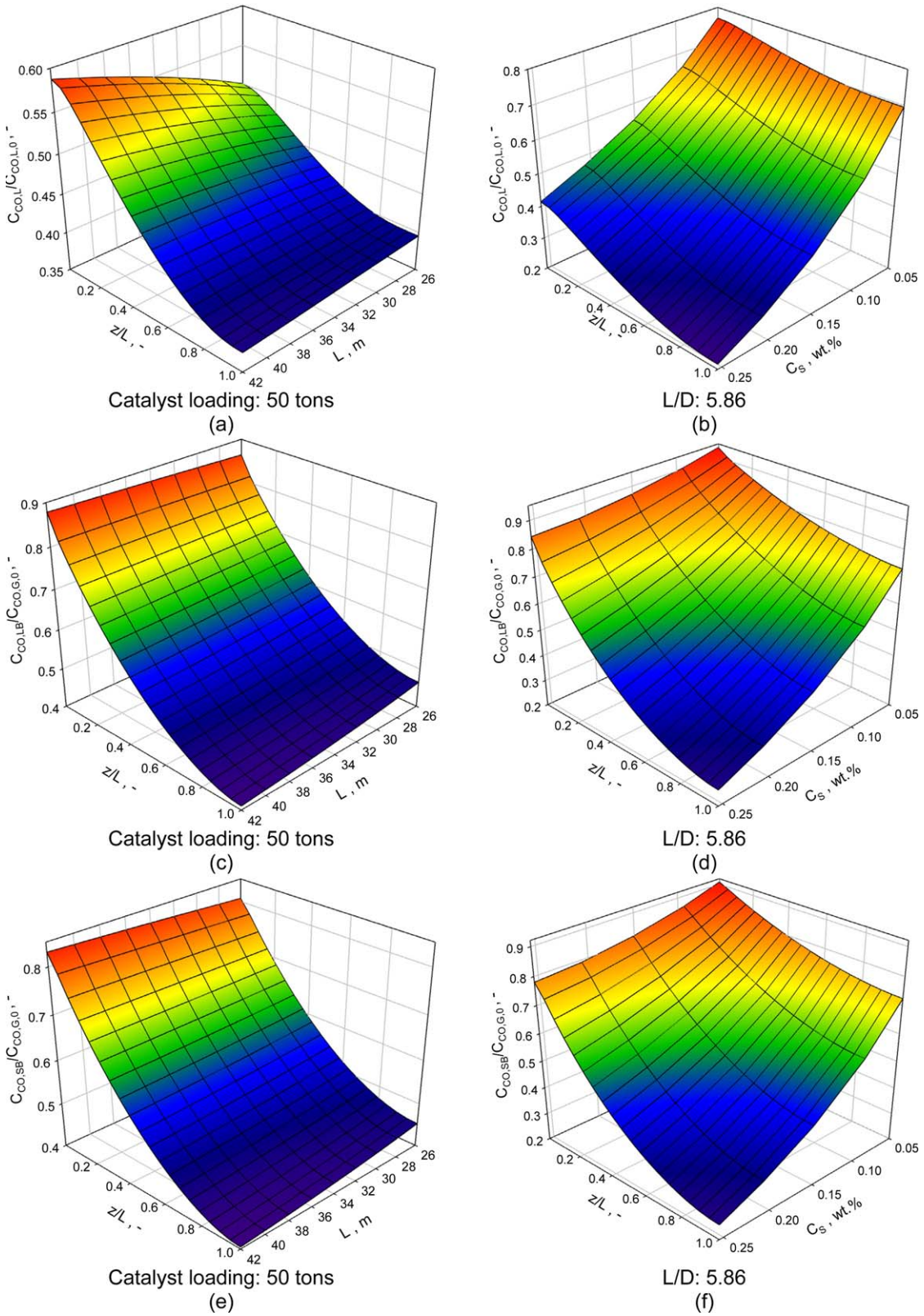

Figure 12. Effect of catalyst concentration and reactor height on the concentration profiles of CO in the different phases: (a) and (b) for liquid phase; (c) and (d) for large gas bubbles-pseudophase; (e) and (f) for small gas bubbles pseudophase.

[Color figure can be viewed in the online issue, which is available at wileyonlinelibrary.com.]

operating conditions listed in Table 22, a short reactor would be better option to minimize the iron-based catalyst deactivation while increasing the C_{5+} products yield.

Assuming that the syncrude from this ID SBCR would undergo an upgrading process similar to that used in the Oryx GTL plant in Qatar,[31] with hydrocracking selectivities

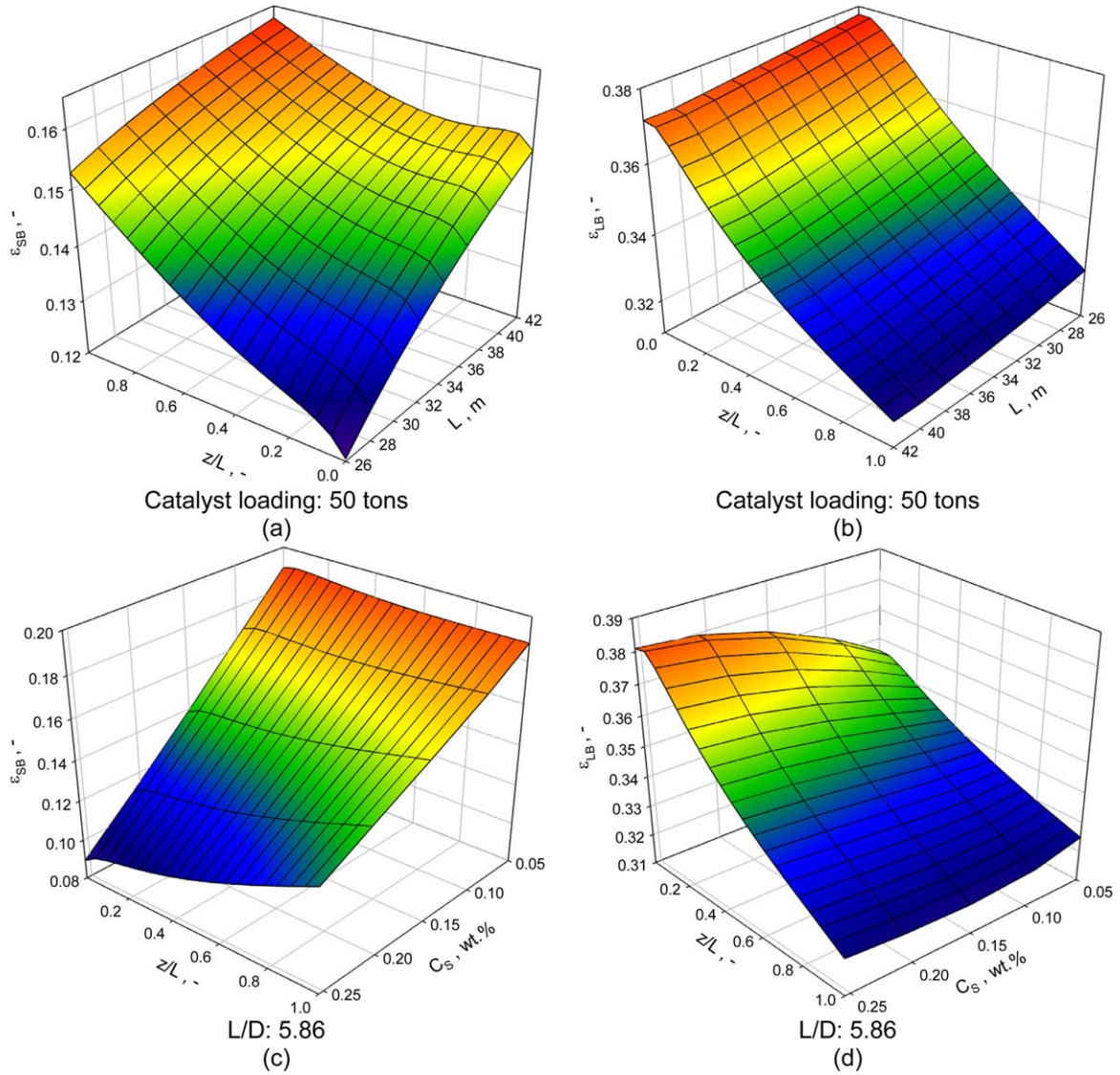

Figure 13. Effect of catalyst concentration and reactor height on the gas holdup profiles: (a) and (c) for small gas bubbles; (b) and (d) for large gas bubbles.

[Color figure can be viewed in the online issue, which is available at wileyonlinelibrary.com.]

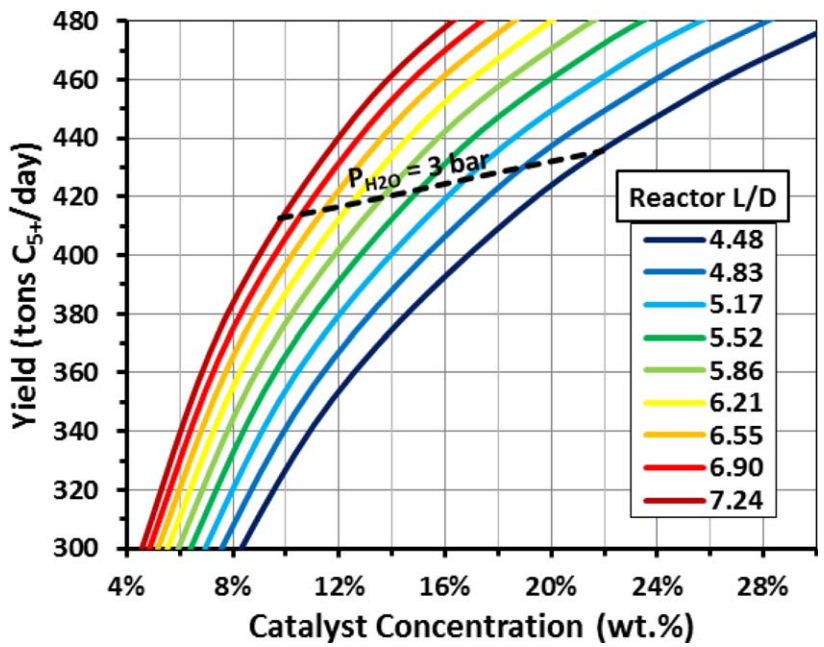

Figure 14. Effect of catalyst concentration and reactor height on C_{5+} products yield.

[Color figure can be viewed in the online issue, which is available at wileyonlinelibrary.com.]

as those reported for an LTFT wax by Leckel,[56] the C_{5+} products yield was found to vary from 2700 to 4734 barrel/day (bpd). More specifically, the yields of naphtha (C_5–C_{10}) and distillate (C_{11}–C_{22}) blends were 1484–2404 bpd and 1216–2330 bpd, respectively. It should also be noted that significant yields of C_1–C_4, representing about 25.5 wt % of the total hydrocarbon products, were produced. Those products have properties similar to synthetic natural gas and liquefied petroleum gas and amounts of about 6296–8269 Nm^3/h (5.34–7.01 MMscfd) and 2349–2974 bpd, respectively.

Concluding Remarks

The hydrodynamic and mass-transfer parameters for N_2 and He/N_2 gaseous mixtures were measured in an actual molten reactor wax in the absence and presence of iron-based catalyst concentrations up to 45 wt % using our pilot-scale (0.29 m) SBCR. The effects of pressure, temperature, superficial gas velocity, catalyst concentration, and gas nature on these parameters were investigated and their behaviors were qualitatively found to be mostly similar to those reported in the literature for FT liquids. A comparison of the experimental data obtained in the pilot scale SBCR with the molten reactor wax and a light FT cut indicated that the different behaviors are most likely due to the difference between the viscosities of the liquids and the presence of a significant amount of alkenes and oxygenates in the molten reactor wax. The experimental data for the gas holdup, large gas bubbles holdup, Sauter mean bubble diameter of large and small gas bubbles, and the volumetric gas-liquid mass-transfer coefficients obtained in this study were compared with the predictions of available literature correlations. With the exception of the correlation of Behkish et al.[49] for large gas bubbles holdup, new correlations were developed to predict the measured data with good accuracy. The selected correlations were subsequently included, along with FT and WGS kinetic expressions for the iron based catalyst, in a comprehensive reactor model for a large scale FT SBCR.

Modeling was conducted to predict the effects of catalyst concentration and reactor height (or L/D ratio) on the water partial pressure, which is the main cause of iron-based catalyst deactivation, the H_2 and CO conversions and the C_{5+} products yield. It was found that the catalyst concentration has much more impact on the reactor performance than the reactor height and therefore a short reactor would provide the best option to minimize catalyst deactivation, while increasing the products yield. The modeling results indicated that to avoid rapid deactivation of the iron-based catalyst, at a reactor L/D of 4.48, the catalyst concentration should be <22 wt %, whereas at a reactor L/D of 7.24, the catalyst concentration should be <10 wt %. Under these two conditions, the H_2 conversions were limited to 49.4 and 48.4% and those for CO were limited to 69.3 and 62.8%. Also, the C_{5+} products yields were 435.6 and 412.7 ton/day, respectively. Thus, under the conditions used in our model, the ID FT SBCR used should operate in the kinetically controlled regime with an L/D of 4.48 and a catalyst concentration of 22 wt % to maximize C_{5+} products yield while minimizing the iron-based catalyst deactivation. However, one may argue that high solid concentrations could translate into a more challenging wax/catalyst separation and a tall reactor would entail higher capital cost.

Acknowledgment

The authors would like to thank the National Institute of Clean-and-low-carbon Energy (NICE), China, for the financial support and for providing the catalyst particles and reactor wax.

Notation

a = FT kinetic coefficient, dimensionless
A = Cross-sectional area of the reactor, m^2
b = WGS kinetic coefficient, dimensionless
AARE = Absolute average relative error: $\left(\frac{1}{n}\sum_1^n \left|\frac{\text{Pred.}-\text{Exp.}}{\text{Exp.}}\right|\times 100\%\right)$
ARE = Average relative error $\left(\frac{1}{n}\sum_1^n \left|\frac{\text{Pred.}-\text{Exp.}}{\text{Exp.}}\right|\times 100\%\right)$
C^* = Equilibrium concentration (solubility) in the liquid phase, $mol\cdot m^{-3}$
C_L = Concentration in the liquid phase, $mol\cdot m^{-3}$
C_S = Concentration of solid particles in the slurry phase, wt %
C_P = Concentration of solid particles in the slurry phase, $kg\cdot m^{-3}$
C_V = Volumetric concentration of solid particles in the slurry phase, vol %
d_{32} = Sauter-mean gas bubbles diameter, m
D_C = Column diameter, m
D_L = Diffusivity of dissolved gas, $m^2\cdot s^{-1}$
ΔH_{cell} = Height difference between 2 sampling ports, m
ΔP_{cell} = Differential pressure between 2 sampling ports, Pa
g = Acceleration due to gravity, 9.81 $m\cdot s^{-2}$
H_C = Column Height, m
k_{FT} = FT kinetic rate constant, $mol\cdot kg^{-1}\ s^{-1}\ Pa^{-1}$
k_La = Volumetric liquid-side mass-transfer coefficient (based on unit volume of liquid or slurry), s^{-1}
k_{WGS} = WGS kinetic rate constant, $mol\cdot kg^{-1}\ s^{-1}$
K_P = WGS equilibrium constant, dimensionless
MMscfd = Million ft^3/day at standard conditions: 60°F (15.56°C), 14.696 psia (101325 Pa)
M_W = Molecular weight, kg/kmol
n_b = Number of gas bubbles, -
P = Pressure, bar
P_V = Liquid-phase vapor pressure, bar
t = Time, s
SD(AARE) = Standard deviation of AARE $\left(\sqrt{\frac{1}{n}\sum_1^n (\text{Absolute Relative Error}_i-\text{AARE})^2}\right)\times 100\%$
SD(ARE) = Standard deviation of ARE $\left(\sqrt{\frac{1}{n}\sum_1^n (\text{Relative Error}_i-\text{ARE})^2}\right)\times 100\%$
T = Temperature, K
U_b = Gas bubble rise velocity, $m\cdot s^{-1}$
U_G = Superficial gas velocity, $m\cdot s^{-1}$
V_t = Terminal velocity of single particle in stagnant liquid, $m\cdot s^{-1}$
X = Weight fraction of the primary liquid in the mixture (See Behkish et al.[49])
y = Mole fraction of gas component, -

Greek letters

α = ASF model chain growth probability, -
ε = Holdup, -
Γ = Gas sparger coefficient (See Behkish et al.[49])
μ = Viscosity, mPa·s
ρ = Density, kg/m^3
σ = Surface tension, N/m

Subscripts

b = Gas bubbles
c = Column
G = Gas phase
L = Liquid phase
LB = Large gas bubbles pseudophase
P = Particles

S = Solid
SB = Small gas bubbles pseudophase
w = water

Literature Cited

1. Dry ME. Chemical concepts used for engineering purposes. In: Fischer-Tropsch Technology, Steynberg AP, Dry ME, editors. Elsevier Science: Amsterdam, 2004:196–257.
2. Dry ME. The Fischer-Tropsch process: 1950-2000. *Catal Today*. 2002;71(3–4):227–241.
3. van der Laan GP, Beenackers AACM, Krishna R. Multicomponent reaction engineering model for Fe-catalyzed Fischer-Tropsch synthesis in commercial scale slurry bubble column reactors. *Chem Eng Sci*. 1999;54(21):5013–5019.
4. Callaghan CA. *Kinetics and Catalysis of the Water-Gas-Shift Reaction: A Microkinetic and Graph Theoretic Approach*. Worcester: Worcester Polytechnic Institute, 2006.
5. Steynberg AP, Dry ME, Davis BH, Breman BB. Fischer-Tropsch reactors. In: Fischer-Tropsch Technology, Steynberg A, Dry M, editors. Elsevier Science: Amsterdam, 2004:64–194.
6. Wilkinson PM, Spek AP, van Dierendonck LL. Design parameters estimation for scale-up of high-pressure bubble columns. *AIChE J*. 1992;38:544–554.
7. Moustiri S, Hebrard G, Thakre S, Roustan M. A unified correlation for predicting liquid axial dispersion coefficient in bubble columns. *Chem Eng Sci*. 2001;56:1041–1047.
8. Deckwer W-D, Louisi Y, Zaidi A, Ralek M. Hydrodynamic properties of the Fischer-Tropsch slurry process. *Ind Eng Chem Process Des Dev*. 1980;19(4):699–708.
9. Bukur D, Patel S, Daly J. Gas holdup and solids dispersion in a three phase slurry bubble column. *AIChE J*. 1990;36:1731–1735.
10. Bukur D, Daly J, Patel S. *Hydrodynamics of the Three-Phase Slurry Fischer-Tropsch Bubble Column Reactors, Final Report No. DOE/PC/90012-10*. US Department of Energy: Pittsburgh, Pennsylvania, 1990.
11. Bukur DB, Daly JG, Patel SA, Raphael ML, Tatterson GB. *Hydrodynamics of Fischer-Tropsch Synthesis in Slurry Bubble Column Reactors, Final Report No. DOE/iPC/70027-10*. U.S. Department of Energy: Washington, DC, 1987.
12. Bukur DB, Daly JG. Gas hold-up in bubble columns for Fischer-Tropsch synthesis. *Chem Eng Sci*. 1987;42:2967–2969.
13. Daly JG, Patel SA, Bukur DB. Measurement of gas holdups and Sauter mean bubble diameters in bubble column reactors by dynamics gas disengagement method. *Chem Eng Sci*. 1992;47(13–14):3647–3654.
14. Patel SA, Daly JG, Bukur DB. Bubble-size distribution in Fischer-Tropsch-derived waxes in a bubble column. *AIChE J*. 1990;36(1):93–105.
15. Krishna R, Swart JWAD, Ellenberger J, Martina GB, Maretto C. Gas holdup in slurry bubble columns: effect of column diameter and slurry concentration. *AIChE J*. 1997;43:311–316.
16. Vandu CO, Krishna R. Volumetric mass transfer coefficients in slurry bubble columns operating in the churn-turbulent flow regime. *Chem Eng Process: Process Intensification*. 2004;43:987–995.
17. Woo K-J, Kang S-H, Kim S-M, Bae J-W, Jun K-W. Performance of a slurry bubble column reactor for Fischer-Tropsch synthesis: determination of optimum condition. *Fuel Process Technol*. 2010;91(4):434–439.
18. Behkish A, Lemoine R, Sehabiague L, Oukaci R, Morsi BI. Gas holdup and bubble size behavior in a large-scale slurry bubble column reactor operating with an organic liquid under elevated pressures and temperatures. *Chem Eng J*. 2007;128(2–3):69–84.
19. Behkish A, Men Z, Inga JR, Morsi BI. Mass transfer characteristics in a large-scale slurry bubble column reactor with organic liquid mixtures. *Chem Eng Sci*. 2002;57(16):3307–3324.
20. Sehabiague L, Morsi BI. Hydrodynamic and mass transfer characteristics in a large-scale slurry bubble column reactor for gas mixtures in actual Fischer–Tropsch cuts. *Int J Chem Reactor Eng*. 2013;11:1–20.
21. de Swart JWa, Krishna R. Simulation of the transient and steady state behaviour of a bubble column slurry reactor for Fischer–Tropsch synthesis. *Chem Eng Process: Process Intensification*. 2002;41:35–47.
22. Rados N, Al-Dahhan MH, Dudukovic MP. Modeling of the Fischer–Tropsch synthesis in slurry bubble column reactors. *Catal Today*. 2003;79–80:211–218.
23. Danckwerts PV. Continuous flow systems: distribution of residence times. *Chem Eng Sci*. 1953;2(1):1–13.
24. Sehabiague L, Lemoine R, Behkish A, Heintz Y, Sanoja M, Oukaci R, Morsi BI. Modeling and optimization of a large-scale slurry bubble column reactor for producing 10,000 bbl/day of Fischer-Tropsch liquid hydrocarbons. *J Chin Inst Chem Eng*. 2008;39(2):169–179.
25. Sehabiague L, Morsi BI. Modeling and simulation of a Fischer–Tropsch slurry bubble column reactor using different kinetic rate expressions for iron and cobalt catalysts. *Int J Chem Reactor Eng*. 2013;11(1):1–22.
26. Rakymkul Y. *Solubilities and Mass Transfer Coefficients of Gases in Heavy Synthetic Hydrocarbon Liquids*. Pittsburgh: University of Pittsburgh, 2011.
27. Marano JJ, Holder GD. General equation for correlating the thermophysical properties of n -Paraffins, n -Olefins, and other homologous series. 2. Asymptotic behavior correlations for PVT properties. *Ind Eng Chem Res*. 1997;36(5):1895–1907.
28. Marano JJ, Holder GD. A general equation for correlating the thermophysical properties of n -Paraffins, n -Olefins, and Other homologous series. 3. Asymptotic behavior correlations for thermal and transport properties. *Ind Eng Chem Res*. 1997;36(6):2399–2408.
29. Deckwer WD, Serpemen Y, Ralek M, Schmidt B. Modeling the Fischer-Tropsch synthesis in the slurry phase. *Ind Eng Chem Process Des Dev*. 1982;21(2):231–241.
30. Inga JR, Morsi BI. Effect of operating variables on the gas holdup in a large-scale slurry bubble column reactor operating with an organic liquid mixture. *Ind Eng Chem Res*. 1999;38(3):928–937.
31. de Klerk A. *Fischer-Tropsch Refining*. Weinheim: Wiley-VCH Verlag & Co. KGaA, 2012.
32. Wilke CR, Chang P. Correlation of diffusion coefficients in dilute solutions. *AIChE J*. 1955;1:264–270.
33. Bukur DB, Patel SA, Matheo R. Hydrodynamic studies in Fischer-Tropsch derived waxes in a bubble column. *Chem Eng Commun*. 1987;60(1–6):63–78.
34. Reilly IG, Scott DS, Debruijn TJW, Macintyre D. The role of gas phase momentum in determining gas holdup and hydrodynamic flow regimes in bubble column operations. *Can J Chem Eng*. 1994;72:3–12.
35. Sehabiague L. *Modeling, Scaleup and Optimization of Slurry Bubble Column Reactors for Fischer-Tropsch Synthesis,* Doctoral Dissertation. Department of Chemical and Petroleum Engineering, University of Pittsburgh: Pittsburgh, Pennsylvania, 2012.
36. Kemoun A, Ong BC, Gupta P, Al-Dahhan H, Dudukovic MP. Gas holdup in bubble columns at elevated pressure via computed tomography. *Int J Multiphase Flow*. 2001;27(5):929–946.
37. Gandhi AB, Joshi JB, Jayaraman VK, Kulkarni BD. Development of support vector regression (SVR)-based correlation for prediction of overall gas hold-up in bubble column reactors for various gas-liquid systems. *Chem Eng Sci*. 2007;62(24):7078–7089.
38. Urseanu MI, Guit RPM, Stankiewicz A, van Kranenburg G, Lommen JHGM. Influence of operating pressure on the gas hold-up in bubble columns for high viscous media. *Chem Eng Sci*. 2003;58(3–6):697–704.
39. Akita K, Yoshida F. Gas holdup and volumetric mass transfer coefficient in bubble columns. Effects of liquid properties. *Ind Eng Chem Process Des Dev*. 1973;12:76–80.
40. Koide K, Takazawa A, Komura M, Matsunaga H. Gas holdup and volumetric liquid-phase mass transfer coefficient in solid-suspended bubble columns. *J Chem Eng Jpn*. 1984;17:459–466.
41. Reilly IG, Scott DS, de Bruijn TJW, Jain A, Piskorz J. A correlation for gas holdup in turbulent coalescing bubble columns. *Can J Chem Eng*. 1986;64:705–717.
42. Dharwadkar SV, Sawant SB, Joshi JB. Gas hold-up in highly viscous pseudoplastic non-newtonian solutions in three phase sparged reactors. *Can J Chem Eng*. 1987;65(3):406–411.
43. Krishna R, van Baten JM, Urseanu MI, Ellenberger J. Design and scale up of a bubble column slurry reactor for Fischer-Tropsch synthesis. *Chem Eng Sci*. 2001;56(2):537–545.
44. Krishna R, Sie ST. Design and scale-up of the Fischer-Tropsch bubble column slurry reactor. *Fuel Process Technol*. 2000;64(1):73–105.
45. Krishna R, Urseanu MI, van Baten JM, Ellenberger J. Rise velocity of a swarm of large gas bubbles in liquids. *Chem Eng Sci*. 1999;54(2):171–183.
46. Fukuma M, Muroyama K, Yasunishi A. Specific gas-liquid interfacial area and liquid-phase mass transfer coefficient in a slurry bubble column. *J Chem Eng Jpn*. 1987;20:321–324.
47. Wilkinson PM, Haringa H, van Dierendonck LL. Mass transfer and bubble size in a bubble column under pressure. *Chem Eng Sci*. 1994;49(9):1417–1427.

48. Lemoine R, Morsi BI. Hydrodynamic and mass transfer parameters in agitated reactors part II: gas-holdup, Sauter mean bubble diameters, volumetric mass transfer coefficients, gas-liquid interfacial areas, and liquid-side mass transfer coefficients. *Int J Chem Reactor Eng*. 2005;3(3):1166.
49. Behkish A, Lemoine R, Oukaci R, Morsi BI. Novel correlations for gas holdup in large-scale slurry bubble column reactors operating under elevated pressures and temperatures. *Chem Eng J*. 2006; 115(3):157–171.
50. Krishna R, Ellenberger J. Gas holdup in bubble column reactors operating in the churn-turbulent flow regime. *AIChE J*. 1996;42(9): 2627–2634.
51. Nedeltchev S, Schumpe A. New approaches for theoretical estimation of mass transfer parameters in both gas-liquid and slurry bubble columns. In: El-Amin M, editor. *Mass Transfer in Multiphase Systems and its Applications*. InTech: Rijeka, Croatia, 2011.
52. Lemoine R, Morsi BI. An algorithm for predicting the hydrodynamic and mass transfer parameters in agitated reactors. *Chem Eng J*. 2005;114(1–3):9–31.
53. Donnelly TJ, Yates IC, Satterfield CN. Analysis and prediction of product distributions of the Fischer-Tropsch Synthesis. *Energy Fuels*. 1988;2(6):734–739.
54. Chang J, Bai L, Teng B, Zhang R, Yang J, Xu Y, Xiang H, Li Y. Kinetic modeling of Fischer–Tropsch synthesis over Fe-Cu-K-SiO2 catalyst in slurry phase reactor. *Chem Eng Sci*. 2007;62(18–20):4983–4991.
55. Wang Y, Fan W, Liu Y, Zeng Z, Hao X, Chang M, Zhang C, Xu Y, Xiang H, Li Y. Modeling of the Fischer-Tropsch synthesis in slurry bubble column reactors. *Chem Eng Process: Process Intensification*. 2008;47(2):222–228.
56. Leckel D. Selectivity effect of oxygenates in hydrocracking of Fischer-Tropsch waxes. *Energy Fuels*. 2007;21(2):662–667.

Manuscript received Nov. 18, 2014, and revision received June 1, 2015.